

## Kinematics of Circumgalactic Gas: Feeding Galaxies and Feedback

CRYSTAL L. MARTIN<sup>1</sup>

STEPHANIE H. HO<sup>1</sup>

GLENN G. KACPRZAK<sup>2</sup>

CHRISTOPHER W. CHURCHILL<sup>3</sup>

<sup>1</sup>*Department of Physics, University of California, Santa Barbara, Santa Barbara, CA 93106, USA*

<sup>2</sup>*Center for Astrophysics and Supercomputing, Swinburne University of Technology, Hawthorn, Victoria 3122, Australia*

<sup>3</sup>*Department of Astronomy, New Mexico State University, Las Cruces, NM 88003, USA*

(Received April 29, 2019)

### ABSTRACT

We present observations of 50 pairs of redshift  $z \approx 0.2$  star-forming galaxies and background quasars. These sightlines probe the circumgalactic medium (CGM) out to half the virial radius, and we describe the circumgalactic gas kinematics relative to the reference frame defined by the galactic disks. We detect halo gas in Mg II absorption, measure the equivalent-width-weighted Doppler shifts relative to each galaxy, and find that the CGM has a component of angular momentum that is aligned with the galactic disk. No net counter-rotation of the CGM is detected within  $45^\circ$  of the major axis at any impact parameter. The velocity offset of the circumgalactic gas correlates with the projected rotation speed in the disk plane out to disk radii of roughly 70 kpc. We confirm previous claims that the Mg II absorption becomes stronger near the galactic minor axis and show that the equivalent width correlates with the velocity range of the absorption. We cannot directly measure the location of any absorber along the sightline, but we explore the hypothesis that individual velocity components can be associated with gas orbiting in the disk plane or flowing radially outward in a conical outflow. We conclude that centrifugal forces partially support the low-ionization gas and galactic outflows kinematically disturb the CGM producing excess absorption. Our results firmly rule out schema for the inner CGM that lack rotation and suggest that angular momentum as well as galactic winds should be included in any viable model for the low-redshift CGM.

*Keywords:* (galaxies:)quasars: absorption lines, galaxies: evolution, galaxies: halos, galaxies: spiral, hydrodynamics, instrumentation: adaptive optics

### 1. INTRODUCTION

The growth of galactic disks requires a nearly continuous gas supply which has been modified by feedback from massive stars. This accretion dilutes the relative number of low metallicity stars (van den Bergh 1962; Worthey et al. 1996; Woolf & West 2012) and substantially lengthens the timescale for building disks (Kennicutt 1983; Papovich et al. 2015). How the sizes of disks

grow as their stellar mass increases depends primarily on the angular momentum of the accreted gas. Observations of disks indicate inside-out growth (Barden et al. 2005; Gogarten et al. 2010; Muñoz-Mateos et al. 2011; González Delgado et al. 2014), consistent with the angular momentum of the accreted gas increasing with cosmic time. The evolution of the stellar specific angular momentum also depends on the stellar feedback history (Governato et al. 2007, 2010; Sijacki et al. 2012; Danovich et al. 2015). Efforts to characterize the mass dependence of the stellar specific angular momentum may constrain the fraction of this angular momentum

retained by galaxies (Fall & Romanowsky 2018). Identifying the circumgalactic gas that feeds the inside-out growth of galactic disks, and its interaction with galactic winds, will be necessary to understand galaxy assembly.

Direct observations of disk accretion remain sparse. Evidence for gas accretion in redshift  $z \approx 0.9 - 2.3$  galaxies has grown steadily in recent years, aided by integral field spectroscopy (Bouché et al. 2013, 2016; Zabl et al. 2019). The disk – halo interface at low redshift, however, has only been well described within a few kpc of the disks (Sancisi et al. 2008). Even for the Milky Way galaxy, much of the infalling gas may go unrecognized because only the highest velocity clouds are easily distinguished from the gas disk (Zheng et al. 2015). Progress measuring physical conditions in the circumgalactic medium (CGM) over the past few years, however, make it timely to systematically study the kinematics of circumgalactic gas now.

These observations have identified a large reservoir of baryons surrounding galaxies. This circumgalactic gas extends to roughly the virial radius (Shull 2014) and contains a substantial fraction of the baryons (Werk et al. 2014; Bregman et al. 2018) and metals (Peeples et al. 2014) associated with the dark matter halo. The larger column densities of the  $O^{+5}$  ion in the CGM of star-forming galaxies compared to passive galaxies (Tumlinson et al. 2011) has generated great interest in the CGM because the processes producing this dichotomy may explain why star formation is quenched in massive halos (Kauffmann et al. 2003; Blanton et al. 2003; Schawinski et al. 2014). In cosmological hydrodynamical simulations, the O VI absorbing gas lies behind the halo accretion shock and is maximal in  $L^*$  galaxies because their virial temperature is close to the temperature  $T \approx 10^{5.5}$  K where the  $O^{+5}$  ionization fraction peaks (Oppenheimer et al. 2016). Feedback from supermassive black holes may suppress the  $O^{+5}$  fraction in the halos of red galaxies relative to the halos of blue galaxies of similar stellar mass (Nelson et al. 2018). The nucleus would not typically still be active by the time its outflow impacted the gas properties at half the virial radius, so differentiating between AGN activity and halo mass is challenging observationally (Berg et al. 2018). Simulations that zoom in on individual galaxies include more physics than cosmological simulations (Hummels et al. 2013; Su et al. 2018). They qualitatively agree that enhanced star formation feedback increases the strength of high-ionization absorption lines as Heckman et al. (2017) observed. Quantitatively, however, the star-formation feedback does not produce enough O VI absorption nor does it permanently quench star formation. A solution may require a completely different schema for the CGM.

Stern et al. (2018) argue, for example, that the O VI absorption occurs beyond the accretion shock, where O VI would be photoionized by the UV background, a low-pressure scenario.

The dichotomy between the CGM properties of blue and red galaxies extends to low-ionization gas. These differences are less widely appreciated because the halos of both star-forming and passive galaxies produce low-ionization absorption-line systems. Large surveys routinely find an excess of strong Mg II absorbers around blue galaxies relative to red galaxies (Lan et al. 2014; Lan & Mo 2018). The large absorption strength requires a substantial velocity spread among velocity components or very large turbulent velocities. We call this the *kinematic dichotomy* between the CGM of star-forming and passive galaxies.

Massive, star-forming galaxies generally have both stellar and gaseous galactic disks (Schawinski et al. 2014). Quasar sightlines near the position angle of the minor axis of a disk detect larger Mg II absorption equivalent widths than do those near the major axis at similar impact parameter (Bordoloi et al. 2011; Bouché et al. 2012; Kacprzak et al. 2012; Lan et al. 2014; Lan & Mo 2018). This minor-axis excess may be associated with galactic winds. Only minor-axis sightlines at very small impact parameters, however, would intersect the outflowing gas that is directly detected in galaxy spectra because the higher covering fraction (and density) of gas at small radii dominates the outflow absorption in galaxy spectra (Martin & Bouché 2009). It has been common to model the trajectory of cool clouds outward from the galaxy to 60 kpc or more (Bouché et al. 2012; Gauthier & Chen 2012; Kacprzak et al. 2014; Schroetter et al. 2016), but this interpretation is in direct conflict with hydrodynamical simulations. Individual clouds in the hot, supersonic wind are destroyed over spatial scales of just a few kiloparsecs in hydrodynamical simulations (Scannapieco & Brüggén 2015; Brüggén & Scannapieco 2016; Schneider & Robertson 2017). Other processes, including cooling hot winds (Wang 1995; Martin et al. 2015; Thompson et al. 2016) and the interaction of hot winds with the CGM (Lochhaas et al. 2018; Su et al. 2018) for example, might produce low-ionization gas that explains the excess minor-axis absorption. A comprehensive look at the relationship between galaxy properties and CGM kinematics would provide additional insight.

The kinematics of galactic disks are rarely measured for the hosts of quasar absorption-line systems. In their exploratory study, Steidel et al. (2002) measured galactic rotation curves for a few galaxies at  $z \approx 0.5$ . Remarkably, the Doppler shift of the galactic rotation often had the same sign as the velocity offset of the Mg II

absorption. Corotation suggested an extended gas disk, but simple disk models did not explain the large velocity width of the absorption systems (Kacprzak et al. 2010, 2011). This linewidth problem does not exclude an extended gas disk contributing a velocity component to a strong Mg II system, as seen for example in one low impact-parameter sightline passing through the halo of a Milky-Way-like galaxy at  $z = 0.413$  (Diamond-Stanic et al. 2016). Multiple quasar sightlines through the halo of a very nearby spiral galaxy also detect absorption best described by a disk-like distribution of gas approximately planar to the observed H I disk yet draw attention to the noise from additional velocity components (Bowen et al. 2016). Multiple sightlines through the same halo can rarely be observed with current facilities however.

Our *Quasars Probing Galaxies* program targets quasars fortuitously located behind redshift  $z \approx 0.2$  blue galaxies, detects low-ionization Mg II (and sometimes Mg I) absorption near the galaxy redshift, and characterizes the kinematics of the circumgalactic gas relative to the galactic reference frame. The galaxy sample is more homogeneous than those presented previously, allowing us to stack the galaxies and produce a multiple-sightline description of the average CGM kinematics. We presented 15 sightlines within  $30^\circ$  of the major axis in Ho et al. (2017), finding no Mg II systems with Doppler shifts in the opposite sense of the foreground galaxy’s rotation. To better characterize the rotation of the CGM, we have expanded the study to 50 sightlines which sample the full range of azimuthal angle. We also measured rotation curves and obtained high-resolution images to better describe the orientation of the galaxy.

In Section 2 we describe the galaxy properties and the detection of associated quasar absorption-line systems. The uniformity of the galaxy properties allows us to discuss the geometry and kinematics of the average CGM with a large number of sightlines. Section 3 describes the absorption signature of low-ionization CGM relative to the projected galactic disks. Properties of the corotators are compared to large, extended disks in Section 4.1, and we discuss the constraints that minor-axis sightlines place on galactic winds and outflows in Section 4.2. Section 4.3 summarizes the empirical constraints on corotation. Throughout the paper we assume a cosmology with  $H_0 = 67.74 \text{ km s}^{-1} \text{ Mpc}^{-1}$ ,  $\Omega_0 = 0.3089$ , and  $\Omega_\Lambda = 0.691$  (Planck Collaboration et al. 2016). The angular diameter distance at  $z = 0.2$  corresponds an angular scale of 3.30 kpc per arcsecond.

## 2. DATA

We selected galaxy – quasar pairs based on the properties of the foreground galaxies. In contrast, traditional surveys detect absorption-line systems in quasar spectra and then identify the galaxy halo. By selecting the galaxies first, we can study the halos of galaxies with very similar properties. It follows that although a single sightline intersects each galaxy halo, the galaxies can be *stacked* such that we sample the average CGM with 50 sightlines. Registration of the pairs requires measurements that establish the orientation of the galactic disk. In this section we describe these selection criteria and observations, summarize the measured galaxy properties, and then present the absorption line systems associated with the galaxies.

### 2.1. Selection of Galaxy – Quasar Pairs

The rest-frame UV bandpass contains many strong transitions from common ions, but the number of quasars bright enough to observe in the UV from space is small compared to the number accessible with ground-based telescopes in the visible. We therefore restricted the sample to  $z > 0.15$  galaxies in order to redshift the Mg II  $\lambda\lambda 2796, 2803$  doublet longward of the atmospheric limit. We also chose low redshift galaxies because we wanted to spatially resolve morphological features.

These star-forming galaxies have a median redshift of  $z \approx 0.21$  so they are fainter than the Sloan Digital Sky Survey DR9 (SDSS, Ahn et al. (2012)) spectroscopic sample. We used photometric redshifts to select the galaxies but then measured spectroscopic redshifts from our new spectra. These redshift revisions mean that our selection criteria are not strict limits.

Passive, red galaxies were excluded from the galaxy sample using a color cut  $M_u - M_r < 2.0$  (Schawinski et al. 2014). We rejected galaxies with disks observed face-on by requiring the SDSS  $r$ -band semi-minor axis to be less than 0.71 times the length of the semi-major axis. We later obtained higher resolution imaging and revised the disk inclination and position angle measurements for a few galaxies.

Our target galaxies are the subset of this sample with a background quasar brighter than  $u = 18.5$  and impact parameters  $b < 100$  kpc, corresponding to 10-50% of the halo virial radius. We inspected the SDSS DR9 spectra of these quasars, eliminating a few Lyman-limit systems and misidentified stars, and obtained a parent sample of galaxy – quasar pairs. Our observational campaign prioritized pairs with  $b < 60$  kpc.

### 2.2. Observations

Table 1 summarizes our new spectroscopic and imaging observations of 50 galaxy – quasar pairs. Measured properties of the galaxies and associated quasar

**Table 1.** Observations

Target	Keck/LRIS	APO/DIS or Keck/ESI <sup>a</sup>	Keck/NIRC2
	Date (Exposure (s))	Date (Exposure (s))	Date (Exposure (s))
J080507+112208/J080508+112157	2014 Feb 1 (4710/4500)	2017 Mar 22 (7200)	2017 Apr 12 (600)
J081125+093616/J081125+093626	2013 Apr 11 (1840/1800)	...	2017 Jan 26 (600)
J081521+082602/J081521+082623	2014 Feb 1 (2835/2250)	...	2017 Jan 26 (600)
J081708+091750/J081708+091751	2014 Feb 1 (2700/2700)	2017 Jan 7 (3400)	2017 Jan 26 (600)
J084235+565358/J084234+565350	2015 Mar 21 (2700/3520)	...	2017 Jan 26 (600)
J084725+254104/J084723+254105	2015 Mar 22 (3600/3520)	...	2017 Jan 26 (600)
J085215+171137/J085215+171143	2014 May 2 (2700/2640)	...	2017 Jan 26 (600)
J090743+532427/J090745+532421	2015 Mar 21 (3600/3520)	...	2017 Apr 12 (1200)
			2017 Jan 26 (600)
J091954+291345/J091954+291408	2015 Mar 22 (1800/1760)	...	2017 Jan 26 (600)
J092908+350942/J092907+350942	2014 Feb 1 (3810/3600)	...	2017 Jan 26 (600)
J095423+093711/J095424+093648	2013 Apr 11 (1840/1800)	2017 Mar 22 (3000)	2017 Jan 26 (600)
J101711+183237/J101713+183232	2015 Mar 22 (2700/2640)	2017 Mar 21 (7200)	2015 May 6 (300)
J102907+421737/J102907+421752	2015 Mar 22 (2700/2640)	2016 Apr 10 (7200)	2017 Jan 26 (600)
J103643+565119/J103640+565125	2015 Mar 22 (1800/1760)	...	2017 Jan 26 (600)
J104151+174558/J104151+174603	2014 May 2 (2400/2340)	2016 Apr 10 (7000)	2017 Apr 12 (1200)
			2015 May 6 (300)
J104242+164638/J104244+164656	2013 Apr 11 (1240/1200)	...	2015 May 6 (600)
J111238+353920/J111239+353928	2014 Feb 1 (2500/3600)	...	2015 May 6 (600)
J113236+340453/J113235+340428	2013 Apr 11 (1840/1800)	...	2015 May 6 (600)
J114335+284532/J114334+284511	2013 Apr 11 (2760/2700)	...	2017 Jan 26 (600)
J114926+142020/J114927+142002	2013 Apr 11 (1240/1200)	...	2017 Jan 26 (600)
J122413+495515/J122411+495511	2014 May 3 (1800/1760)	...	2017 Jan 26 (600)
J123049+071050/J123049+071036	2015 Mar 21 (3600/3520)	...	2015 May 6 (600)
J123249+433244/J123250+433227	2014 Feb 1 (3720/3600)	2016 May 13 (4200)	2015 May 6 (600)
J123318+103542/J123317+103538	2014 May 3 (1800/1760)	...	2015 May 6 (600)
J124601+173152/J124601+173156	2014 May 3 (2700/2640)	...	2017 Apr 12 (1200)
			2017 Jan 26 (600)
J133541+285324/J133542+285330	2014 Feb 1 (2340/2250)	2016 May 30 (5200)	2015 May 6 (600)
J133740+055211/J133741+055216	2013 Apr 11 (3660/3600)	2017 Feb 22 (5100)	2017 Jan 26 (600)
J135051+250506/J135051+250454	2015 Mar 22 (3600/1800)	2017 Mar 22 (2700)	2017 Apr 12 (600)
J135521+303320/J135522+303324	2014 May 3 (3600/3520)	...	2015 May 6 (600)
J135733+254205/J135734+254204	2014 May 2 (2400/2340)	2015 Mar 25 (3600)	2017 Apr 12 (600)
J140852+245637/J140852+245631	2013 Apr 11 (2760/2700)	...	2017 Apr 12 (600)
J142459+382113/J142501+382100	2014 May 2–3 (1800/1760)	2016 Apr 2 (5100)	2015 May 6 (600)
J142815+585442/J142816+585432	2014 Feb 1 (1320/1320)	...	2017 Apr 12 (600)
J142910+324840/J142911+324824	2013 Apr 11 (1540/1500)	...	...
J143512+360424/J143511+360437	2015 Mar 22 (1800/1760)	...	2015 May 6 (600)
J143603+375138/J143603+375131	2015 Mar 22 (1800/1760)	2016 Jun 6 (2100) (E)	2015 May 6 (600)
J144727+403217/J144727+403206	2014 May 3 (3600/3520)	2016 May 13 (4800)	2017 Apr 12 (600)
J145844+170522/J145844+170514	2015 Mar 22 (1800/1760)	2016 May 30 (4200)	2017 Jan 26 (600)
J150119+155602/J150118+155623	2014 May 3 (3600/3520)	...	2015 May 6 (600)
J150150+553227/J150150+553241	2014 Feb 1 (3400/3000)	...	...
J152027+421519/J152028+421530	2015 Mar 21 (2700/1740)	2016 Apr 2 (4500)	2017 Apr 12 (600)
J153546+391932/J153546+391931	2015 Mar 21 (1800/1740)	2016 Jun 6 (1000) (E)	2015 May 6 (600)
J154454+165703/J154453+165710	2015 Mar 22 (2700/2640)	...	2015 May 6 (600)
J154741+343350/J154741+343357	2014 May 3 (1800/1760)	...	2015 May 6 (600)
J154956+070056/J154956+070044	2013 Apr 11 (1840/1800)	...	2015 May 6 (600)
J155505+362848/J155504+362847	2015 Mar 21 (1800/1760)	2016 Jul 4 (3200)	2017 Apr 12 (600)
J160906+441721/J160907+441734	2015 Mar 21–22 (5400/5280)	...	2017 Apr 12 (600)
J160951+353838/J160951+353843	2014 May 2 (1800/1760)	...	2015 May 6 (600)
J165930+373527/J165931+373528	2013 Apr 11 (2240/2200)	2013 Jul 12 (4400)	2015 May 6 (600)
J171222+291758/J171220+291806	2014 May 2–3 (3600/3520)	...	2015 May 6 (1200)

<sup>a</sup>The label (E) indicates the galaxy spectra were obtained from Keck/ESI instead of APO/DIS. The Keck/ESI observations were conducted through the Keck observing time allocated to the Swinburne University.

absorption-line systems follow in Sections 2.3 and 2.5, respectively. Section 2.4 describes the environments of the target galaxies.

### 2.2.1. Spectroscopy

We spectroscopically observed the quasars using the Low Resolution Imaging Spectrograph (LRIS) at the W. M. Keck Observatory (Oke et al. 1995; Steidel et al. 2004). We designed custom slitmasks in order to simultaneously observe the quasar, target galaxy, and several *filler galaxies* that had SDSS photometric redshifts consistent with the target galaxy, prioritizing the filler galaxies by their luminosity and angular separation from the quasar. The mask position angles were not restricted to the parallactic angle because LRIS has an atmospheric dispersion corrector (Phillips et al. 2006). We configured LRIS with the 1200 line  $\text{mm}^{-1}$  blue grism blazed at 3400 Å, D500 dichroic, and 900 line  $\text{mm}^{-1}$  red grating blazed at 5500 Å. The  $1''.0$  wide slitlets provided a resolution of 105-165  $\text{km s}^{-1}$  FWHM (full width at half maximum intensity) with LRISb and 75-105  $\text{km s}^{-1}$  FWHM on the red side.

Following the procedure discussed in detail by Ho et al. (2017), we removed fixed pattern noise, rejected cosmic rays, and measured the shifts between individual frames. We computed a variance image when these frames were combined. We wavelength calibrated the frames using arc lamp exposures, checked the dispersion solution using night-sky emission lines, and applied small ( $< 25 \text{ km s}^{-1}$ ) zeropoint corrections as warranted. We applied a heliocentric correction and extracted one-dimensional spectra and error spectra. The RMS error in the dispersion solution was  $\lesssim 15 \text{ km s}^{-1}$  over the region covering Mg II.

We measured H $\alpha$  Doppler shifts along the major axis of the target galaxy. If the position angle of the LRIS slitlit was not within  $30^\circ$  of the major axis, then we obtained longslit spectroscopy with the Apache Point Observatory 3.5 m telescope. We configured the blue and red sides of the Double Imaging Spectrograph with 1200 lines  $\text{mm}^{-1}$  gratings blazed at 4400 Å and 7300 Å, respectively. We obtained a resolution of 50  $\text{km s}^{-1}$  with a  $1''.5$  slit width. We integrated long enough to detect H $\alpha$  across many spatial resolution elements. Table 1 provides the exposure times and observation dates. Ho et al. (2017) describe the data reduction procedure.

The *Cosmic Origins Spectrograph* on HST (Green et al. 2012) has observed two of the 50 quasars we observed with LRIS. We retrieved the G130M observations from the HST archive for J155504+362847 (GO 11598; PI Tumlinson) and J165931+373528 (GO 14264; PI Kacprzak). All exposures covering the O VI doublet were compared. Absorption in O VI is detected near the redshift of J155505+362848. The O VI doublet is not clearly detected at the redshift of J165930+373527.

### 2.2.2. High Resolution Imaging

High resolution images were obtained using the quasar as the tip-tilt reference for the Laser Guide Star Adaptive Optics system (Wizinowich et al. 2006) on Keck II. We configured the NIRC2 camera in the wide field mode providing an average plate scale of  $0''.04 / \text{pix}$  over the  $1024 \times 1024$  InSb array. We observed with the *Ks* filter and 20 s integrations, nodding the telescope between coadditions. We choose a camera position angle and dither pattern that kept the galaxy – quasar pair off the bad quadrant of the detector. The pixels undersample the diffraction limit at  $2.146 \mu\text{m}$ , so we also applied sub-pixel dithers at each nod position.

We removed fixed pattern noise and drizzled the frames using the pipeline provided by the UCLA/Galactic center group (Ghez et al. 2008). The point-spread function (psf) estimated from the quasar profile has a median full width at half maximum intensity of  $0''.13$ . Data taken during periods of high winds has a psf elongated in the altitude direction which we attribute to wind shake. We increased the number of coadditions under these challenging conditions, but the low bandwidth wavefront sensor did not always close the loop. We flux calibrated the images using a combination of A0 star observations and the 2MASS *Ks* magnitudes of the quasars. Table 2 provides the new *Ks*-band galaxy photometry.

We imaged 9 of the target galaxies with the Hubble Space Telescope (GO14754). Short exposures with WFC3/UV were obtained through the F390W and F814W filters. The data were reduced and calibrated with the WFC3 calibration pipeline and then drizzled. Cosmic ray removal followed the steps described in Ho et al. (2019, in prep), which describes properties of the disks probed by major-axis sightlines.

Table 2. Properties of Target Galaxies

Galaxy	RA (J2000)	DEC (J2000)	z	PA ( $^{\circ}$ )	$\iota$ ( $^{\circ}$ )	$v_{\infty}$ ( $\text{km s}^{-1}$ )	$R_{RC}$ (kpc)	Ks (mag)	NUV (mag)	FUV (mag)	$M_*$ ( $M_{\odot}$ )	$M_u$	$M_r$	$M_h$ ( $M_{\odot}$ )	$r_v$ (kpc)
(1)	(2)	(3)	(4)	(5)	(6)	(7)	(8)	(9)	(10)	(11)	(12)	(13)	(14)	(15)	(16)
J080507.60+112208.3	08:05:07.60	+11:22:08.36	0.21811	32.5	45.6	190	3.28	$18.71 \pm 0.03$	...	...	9.74	-19.45	-20.70	11.47	154
J081125.76+093616.9	08:11:25.76	+09:36:16.93	0.20118	96.8	66.4	...	...	$17.58 \pm 0.02$	...	...	10.46	-19.57	-21.27	12.05	243
J081521.69+082602.1	08:15:21.69	+08:26:02.11	0.25055	97.7	57.5	...	...	$17.53 \pm 0.08$	...	...	10.62	-20.60	-22.03	12.31	288
J081708.29+091750.3	08:17:08.29	+09:17:50.31	0.17395	-28.8	46.0	80	2.44	$16.82 \pm 0.01$	...	...	10.56	-19.44	-21.42	12.18	273
J084235.98+565358.7	08:42:35.98	+56:53:58.78	0.21824	-133.0	59.6	...	...	$19.22 \pm 0.05$	$\geq 22.24$	$\geq 21.68$	9.64	-18.86	-20.36	11.42	148
J084725.06+254104.7	08:47:25.06	+25:41:04.70	0.19591	110.2	52.1	115	2.35	$18.24 \pm 0.04$	$\geq 23.96$	$\geq 23.76$	9.90	-18.12	-20.24	11.56	166
J085215.36+171137.0	08:52:15.36	+17:11:37.07	0.16921	-159.7	76.7	200	2.68	$18.36 \pm 0.02$	...	...	9.81	-18.89	-20.26	11.50	162
J090743.44+532427.2	09:07:43.44	+53:24:27.20	0.18587	167.3	48.7	150	2.25	$18.77 \pm 0.20$	$21.61 \pm 0.10$	$22.51 \pm 0.23$	9.71	-18.84	-20.37	11.45	154
J091954.11+291345.3	09:19:54.11	+29:13:45.34	0.23288	-9.7	72.5	250	3.44	$17.14 \pm 0.16$	$21.05 \pm 0.03$	$\geq 21.54$	10.54	-19.82	-21.47	12.18	263
J092908.86+350942.2	09:29:08.86	+35:09:42.21	0.18585	18.1	64.8	...	...	$18.77 \pm 0.08$	...	...	9.78	-18.71	-20.30	11.49	159
J095423.27+093711.0	09:54:23.27	+09:37:11.09	0.20253	-133.0	+51.8	225	1.03	$16.99 \pm 0.02$	$20.91 \pm 0.07$	$21.97 \pm 0.26$	10.43	-19.90	-21.69	12.01	236
J101711.80+183237.6	10:17:11.80	+18:32:37.60	0.18966	-20.1	83.7	165	3.59	$19.36 \pm 0.08$	$\geq 22.16$	...	9.47	-17.79	-19.39	11.34	141
J102907.56+421737.6	10:29:07.56	+42:17:37.64	0.26238	-153.9	50.3	155	2.09	$19.00 \pm 0.14$	$\geq 22.41$	$\geq 21.81$	9.93	-19.63	-21.14	11.59	165
J103643.44+565119.0	10:36:43.44	+56:51:19.00	0.13629	-93.9	58.0	210	1.74	$17.68 \pm 0.04$	$20.93 \pm 0.02$	$21.37 \pm 0.05$	9.94	-18.94	-20.61	11.56	173
J104151.26+174558.7	10:41:51.26	+17:45:58.79	0.14232	-17.4	73.7	75	1.55	$20.44 \pm 0.09$	...	...	8.72	-17.81	-18.70	11.01	113
J104242.75+164638.4	10:42:42.75	+16:46:38.44	0.19610	138.4	54.2	...	...	$17.95 \pm 0.06$	$20.57 \pm 0.19$	$\geq 21.30$	9.99	-19.80	-21.28	11.61	174
J111238.15+353920.4	11:12:38.15	+35:39:20.49	0.24671	135.0	48.5	...	...	$18.50 \pm 0.09$	$\geq 22.31$	$\geq 21.62$	9.91	-19.43	-21.00	11.58	164
J113236.10+340453.0	11:32:36.10	+34:04:53.03	0.22210	112.1	51.5	...	...	$18.13 \pm 0.04$	$20.90 \pm 0.16$	$\geq 21.26$	9.90	-19.69	-21.03	11.56	165
J114335.30+284532.0	11:43:35.30	+28:45:32.00	0.14013	-81.5	50.1	...	...	$17.97 \pm 0.07$	$20.68 \pm 0.30$	$20.97 \pm 0.41$	9.95	-18.94	-20.59	11.57	174
J114926.83+142020.3	11:49:26.83	+14:20:20.35	0.21887	-143.8	52.6	...	...	$17.80 \pm 0.10$	...	...	10.36	-20.14	-21.73	11.94	221
J122413.10+495515.4	12:24:13.10	+49:55:15.43	0.26014	-153.0	+52.8	210	2.49	$17.26 \pm 0.03$	$21.20 \pm 0.07$	$21.79 \pm 0.14$	10.55	-20.32	-22.05	12.20	264
J123049.01+071050.5	12:30:49.00	+07:10:51.56	0.39946	-40.0	37.8	190	1.66	$18.39 \pm 0.03$	$22.66 \pm 0.16$	$\geq 23.62$	10.43	-20.41	-21.94	12.09	224
J123249.06+433244.9	12:32:49.06	+43:32:44.96	0.21479	42.0	-60.2	180	1.80	$17.94 \pm 0.05$	$\geq 21.30$	$\geq 21.33$	10.06	-19.42	-21.12	11.67	179
J123318.80+103542.1	12:33:18.80	+10:35:42.13	0.21040	-100.6	48.7	175	2.13	$18.96 \pm 0.07$	$21.67 \pm 0.11$	$\geq 21.24$	9.56	-19.06	-20.32	11.38	144
J124601.75+173152.1	12:46:01.75	+17:31:52.15	0.26897	-178.1	62.6	60	2.55	$19.83 \pm 0.13$	...	...	9.25	-19.40	-20.15	11.25	127
J133541.46+285324.7	13:35:41.46	+28:53:24.78	0.28301	-7.7	-58.0	175	4.85	$18.74 \pm 0.05$	$21.17 \pm 0.07$	$21.83 \pm 0.15$	9.89	-20.04	-21.20	11.57	160
J133740.48+055211.9	13:37:40.48	+05:52:11.96	0.16178	168.7	57.0	115	2.30	$18.34 \pm 0.08$	$20.76 \pm 0.06$	$\geq 21.12$	9.67	-19.30	-20.62	11.43	154
J135051.70+250506.5	13:50:51.70	+25:05:06.58	0.13709	157.6	50.9	180	2.75	$17.99 \pm 0.18$	$21.31 \pm 0.19$	$21.33 \pm 0.45$	9.72	-18.91	-20.54	11.44	158
J135521.20+303320.4	13:55:21.20	+30:33:20.41	0.20690	80.6	+71.9	...	...	$18.59 \pm 0.16$	$\geq 21.32$	$\geq 21.30$	9.76	-19.20	-20.64	11.48	156
J135733.86+254205.1	13:57:33.86	+25:42:05.14	0.25995	-98.1	44.9	160	2.49	$17.74 \pm 0.07$	...	...	10.22	-19.76	-21.39	11.81	196
J140852.40+245637.3	14:08:52.40	+24:56:37.38	0.16686	-167.8	74.5	...	...	$19.31 \pm 0.06$	...	...	9.55	-18.49	-20.11	11.37	147
J142459.82+382113.3	14:24:59.82	+38:21:13.37	0.21295	-48.6	60.7	190	2.15	$17.90 \pm 0.07$	$21.05 \pm 0.10$	$\geq 21.47$	10.15	-19.58	-21.20	11.73	189
J142815.41+585442.1	14:28:15.46	+58:54:42.23	0.37731	-171.7	66.4	...	...	$19.01 \pm 0.17$	$21.38 \pm 0.19$	$\geq 21.91$	10.10	-20.60	-21.68	11.75	175
J142910.91+324840.2	14:29:10.91	+32:48:40.20	0.26130	96.6	53.9	...	...	...	$21.56 \pm 0.02$	$22.24 \pm 0.19$	10.79	-20.12	-21.99	12.63	366
J143512.93+360424.9	14:35:12.93	+36:04:24.98	0.26225	-102.8	60.3	...	...	$19.50 \pm 0.16$	$\geq 22.06$	$\geq 21.70$	9.73	-18.89	-20.45	11.48	151

Table 2 continued

Table 2 (continued)

Galaxy	RA (J2000)	DEC (J2000)	$z$	PA ( $^{\circ}$ )	$\iota$ ( $^{\circ}$ )	$v_{\infty}$ ( $\text{km s}^{-1}$ )	$R_{RC}$ (kpc)	Ks (mag)	NUV (mag)	FUV (mag)	$M_*$ ( $M_{\odot}$ )	$M_u$ ( $M_{\odot}$ )	$M_r$	$M_h$ ( $M_{\odot}$ )	$r_v$ (kpc)
(1)	(2)	(3)	(4)	(5)	(6)	(7)	(8)	(9)	(10)	(11)	(12)	(13)	(14)	(15)	(16)
J143603.16+375138.5	14:36:03.16	+37:51:38.55	0.31462	-120.0	71.9	260	3.80	18.28 $\pm$ 0.06	...	...	10.32	-20.20	-21.82	11.93	208
J144727.42+403217.8	14:47:27.42	+40:32:17.89	0.24497	134.4	55.2	205	3.58	17.63 $\pm$ 0.07	22.45 $\pm$ 0.16	$\geq$ 23.03	10.30	-19.47	-21.37	11.88	209
J145844.18+170522.2	14:58:44.18	+17:05:22.26	0.21965	8.3	+54.4	225	3.30	17.32 $\pm$ 0.03	21.26 $\pm$ 0.35	$\geq$ 20.89	10.42	-20.01	-21.79	12.01	233
J150119.24+155602.2	15:01:19.24	+15:56:02.25	0.17779	-90.0	60.0	...	...	18.44 $\pm$ 0.09	21.70 $\pm$ 0.13	$\geq$ 21.31	9.75	-18.80	-20.39	11.47	157
J150150.28+553227.5	15:01:50.28	+55:32:27.58	0.15139	-68.9	55.0	...	...	...	$\geq$ 21.75	$\geq$ 22.46	9.17	-17.56	-18.99	11.20	130
J152027.21+421519.3	15:20:27.21	+42:15:19.37	0.21099	93.5	-55.4	220	2.13	16.69 $\pm$ 0.04	$\geq$ 21.99	$\geq$ 21.83	10.58	-19.91	-21.90	12.23	277
J153546.74+391932.2	15:35:46.74	+39:19:32.27	0.25587	21.4	+52.9	215	1.64	17.34 $\pm$ 0.08	...	...	10.57	-20.03	-21.81	12.23	271
J154454.75+165703.7	15:44:54.75	+16:57:03.78	0.20215	-16.5	56.3	...	...	17.91 $\pm$ 0.11	...	...	10.12	-19.88	-21.19	11.71	186
J154741.46+343350.8	15:47:41.46	+34:33:50.86	0.18392	-145.3	59.3	175	1.59	18.10 $\pm$ 0.07	...	...	9.96	-18.86	-20.53	11.59	172
J154956.73+070056.0	15:49:56.73	+07:00:56.09	0.16235	-104.8	+63.0	...	...	19.58 $\pm$ 0.07	...	...	9.28	-18.75	-19.90	11.25	135
J155505.27+362848.4	15:55:05.27	+36:28:48.40	0.18926	132.6	55.2	255	3.59	17.86 $\pm$ 0.09	...	...	10.12	-19.72	-21.10	11.70	187
J160906.72+441721.5	16:09:06.72	+44:17:21.50	0.14732	-141.5	70.1	145	3.19	19.48 $\pm$ 0.33	...	...	9.41	-18.18	-19.79	11.30	141
J160951.62+353838.5	16:09:51.62	+35:38:38.58	0.28940	178.7	65.2	45	2.69	18.98 $\pm$ 0.06	...	...	9.93	-19.95	-21.00	11.60	163
J165930.44+373527.9	16:59:30.44	+37:35:27.90	0.19984	-8.2	-56.8	170	2.72	17.62 $\pm$ 0.04	20.21 $\pm$ 0.17	20.70 $\pm$ 0.31	10.01	-20.38	-21.52	11.63	175
J171222.58+291758.6	17:12:22.58	+29:17:58.67	0.21020	74.0	58.8	...	...	17.42 $\pm$ 0.03	...	...	10.18	-19.68	-21.26	11.76	193

NOTE— Column Descriptions: (1) Target galaxy. (2,3) Coordinates of target galaxy. (4) Emission-line redshift of target galaxy. The redshift corrections were most substantial for J123049.01+071050.5 (0.167  $\rightarrow$  0.39946), J142815.41+585442.1 (0.243  $\rightarrow$  0.37731), and J143603.16+375138.5 (0.20011  $\rightarrow$  0.31462). (5) Position angle of galaxy major axis. (6) Inclination of galactic disk estimated as  $\iota = \arccos(b/a)$ , where  $b$  and  $a$  are the lengths of the semi-minor and semi-major axes, respectively. If the 3D orientation of the disk has been established, then we provide the sign of the inclination. (7) Asymptotic rotation speed of galactic disk. An arctangent model,  $v_{\phi}(R) = 2/\pi v_{\infty} \arctan(R/R_{RC})$ , for the disk was projected onto the sky, convolved with a Gaussian model for the seeing disk, and fit to the Doppler shifts measured along the spectroscopic slit. (8) Scale radius for the rotation curve model. (9) AB magnitude of target galaxy from NIRC2 photometry. (10,11) AB magnitudes of target galaxy from GALEX NUV and FUV photometry. (12) Stellar mass fit to SDSS ugriz, NIRC2 Ks, and GALEX NUV/FUV photometry, except as noted. The stellar population synthesis models have a Chabrier initial mass function and an exponentially decaying SFR. Fits were computed using FAST (Kriek et al. 2009). (13,14) Absolute magnitudes in  $u$  and  $r$  bands from SED fit. (15) Halo mass estimate from abundance matching (Behroozi et al. 2010). We adopt the halo mass that contains an average stellar mass matched to our measured stellar mass. We use the measured spectroscopic redshift for each galaxy. We propagate uncertainties in the measured stellar mass but do not account for the scatter in the stellar mass - halo mass relation. (16) Halo virial radius, defined by the overdensity  $\Delta_{vir}(z) = 18\pi^2 + 82z - 39z^2$  (Bryan & Norman 1998) with respect to the critical density and evaluated at the redshift shown in column 4.

### 2.3. Galaxy Properties

We measured galaxy redshifts from the bright optical emission lines in the red LRIS spectrum. These spectroscopic redshifts supercede the SDSS photometric redshifts, which are not accurate enough for describing the velocity offsets of the circumgalactic gas. Three of the target galaxies had large redshift corrections; see notes to Table 2. These spectroscopic redshifts define the systemic velocity of the target galaxies.

To ensure consistency with the new redshifts, we revised the galaxy rest-frame colors and stellar masses via spectral energy distribution (SED) fitting with FAST (Kriek et al. 2009). We added our new Ks-band photometry to the SDSS *ugriz* photometry obtained from the DR9 PhotoObjAll catalog. Including our *Ks* photometry lowered the stellar mass estimates significantly for five galaxies, effectively requiring younger SEDs. If the galaxy was not blended with the quasar in archival GALEX images, the FUV and NUV magnitudes (often upper limits on the flux) were included in the SED fit. Adding this constraint on the UV slope lowered one of the mass estimates by a factor of two, reddened J084723+254105, moving it into the green valley, but did not change the median  $M_u - M_r$  color of the sample. The broad spectral coverage constrains the stellar masses well, although the meaning of the fitted parameters is different for three targets that turned out to be blends of two galaxies. We note these exceptions in Table 2 where we list the measured galaxy properties and define several derived properties including masses.

Figure 1 shows the resulting color – magnitude and color – mass diagrams. The stellar masses are typical for late-type galaxies at low redshift. The color cut biases the sample median color bluer than the average late-type galaxy with  $10^{10} M_\odot$  of stars. The median halo mass of a target galaxy is  $10^{11.6} M_\odot$ . The halo virial radii have a median value of 170 kpc.

The high-resolution images confirm that the target galaxies have late-type morphologies as expected based on the color selection. The SDSS images accurately determine the disk position angle and axis ratio in many cases. An example is J081708+081750, which is shown in the top panel of Figure 2. The bluest image in F390W resolves flocculent spiral structure that is fairly axisymmetric.

Young stellar populations provide the best contrast between the arms and the underlying stellar disk, so it is surprising that some Ks images detect spiral structure. The middle panel of Figure 2 shows an example, a two-arm spiral pattern in J143606+375138. The two-arm pattern is typical of the arms resolved by our infrared imaging; these arms may be driven by a recent interac-

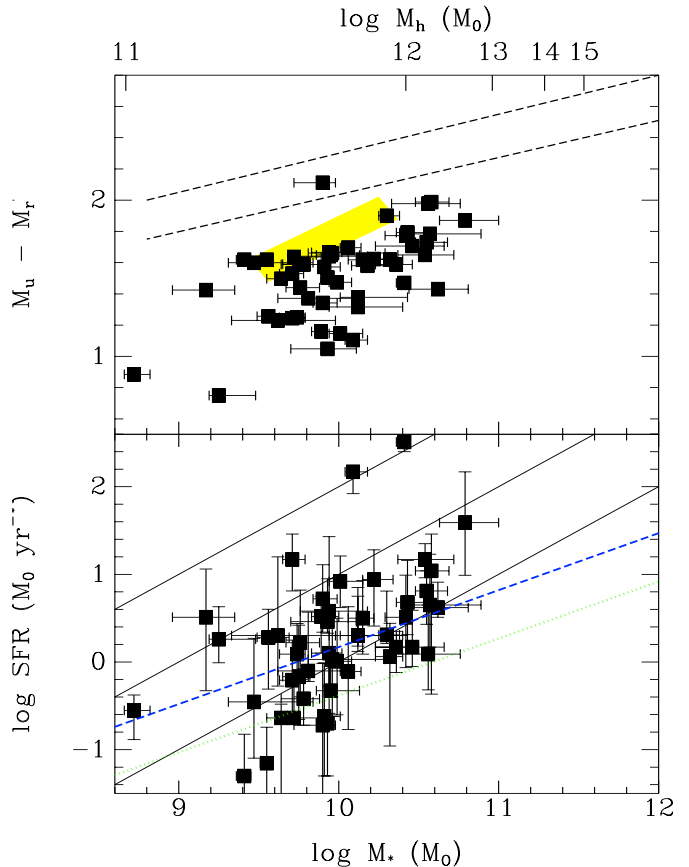


**Figure 1.** Properties of galaxy sample. *Top:* Color – mass diagram for the galaxy sample. The diagonal lines show the green valley defined by all morphological types, and the shaded region shows the peak density of late-type galaxies (Schawinski et al. 2014). The median color ( $M_u - M_r = 1.59$ ) is 0.15 magnitude bluer than the typical late-type galaxy at the median stellar mass ( $\log M_* = 9.94$ ) of our targets. *Bottom:* Solid lines represent specific SFRs of  $10^{-8}$ ,  $10^{-9}$ , and  $10^{-10} \text{ yr}^{-1}$ . The green dotted line denotes the division between star-forming and quiescent galaxies at redshift  $z = 0.2$  (Moustakas et al. 2013). The blue dashed line denotes the main sequence of star formation (Salim et al. 2007).

tion with another galaxy. Resolving spiral arms allows us to discuss the 3D orientation of the disks in Section 4.

Upon close inspection the NIRC2 Ks images often reveal non-axisymmetric structure that was not resolved by the SDSS imaging. These features include faint companions as well as spiral arms. We ran GALFIT (Peng et al. 2010) on the Ks images and found the disk position angles and inclinations typically require revisions of only a few degrees. Table 2 lists the adopted disk position angles and inclinations. The seeing-limited resolution produced catastrophic systemic errors for the orientations of three pairs of blended galaxies. For illustra-

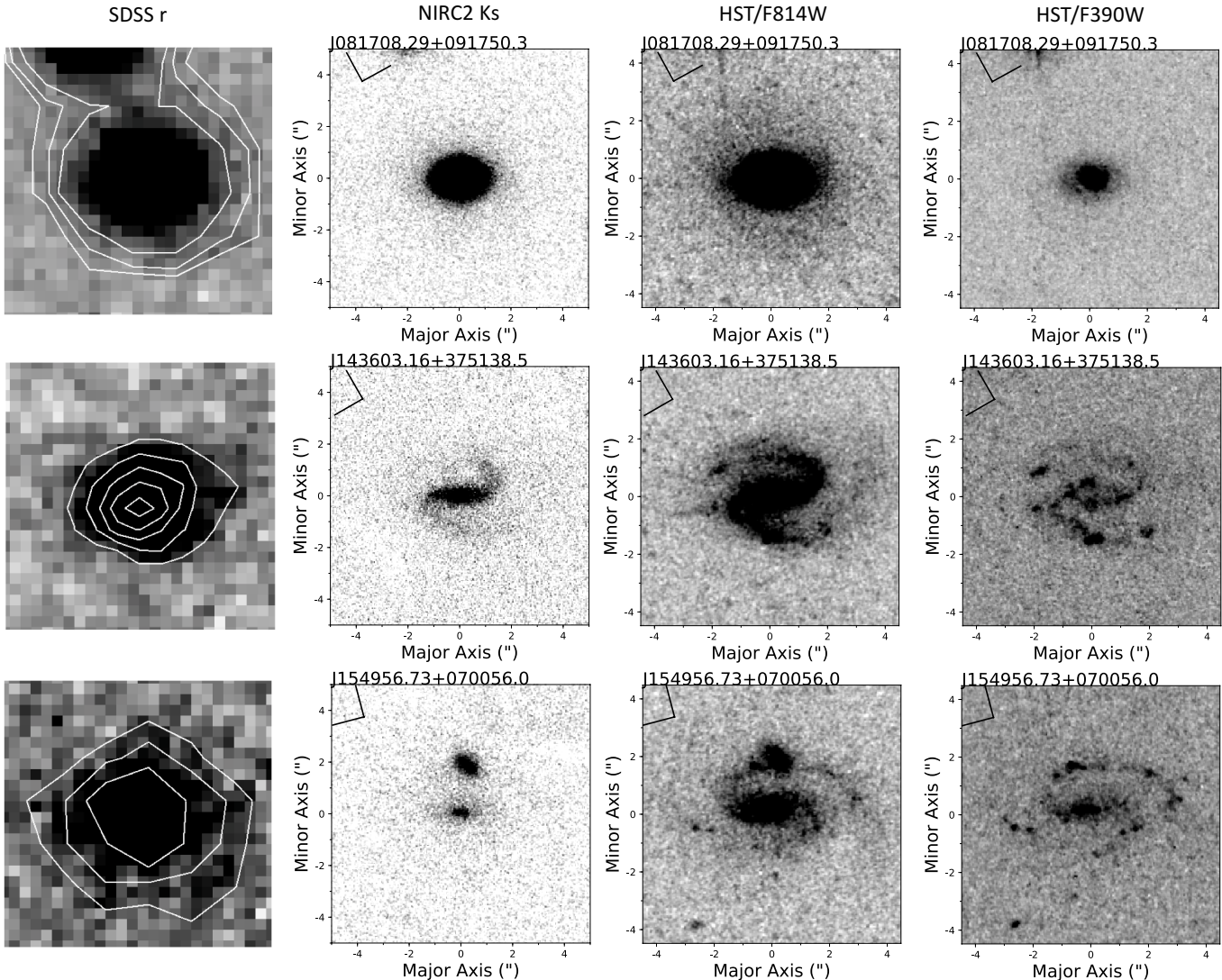


**Figure 2.** Comparison of SDSS, NIRC2/LGSAO, and HST images. *Top:* The position angle and axis ratio of a target galaxy can often be accurately measured from SDSS images. *Middle:* However non-axisymmetric structure can skew the disk orientation measured from SDSS images. The NIRC2/LGSAO *Ks* images detect large-scale, two-arm spiral patterns in roughly 10% of the galaxies. Unsharp masking brings out spiral structure in additional 10% of the *Ks* images. *Bottom:* High-resolution imaging also resolves close pairs of galaxies, allowing us to eliminate large orientation errors. The bluer F390W images emphasize the youngest stellar population, and these images detect spiral structure in  $\approx 90\%$  of the galaxies imaged.

tion, the bottom panel of Figure 2 shows the the NIRC2 *Ks* image of J154956+070056. We adopted the fainter galaxy in the *Ks* image as our target because its coordinates were closer to the SDSS coordinates. Later, the HST images showed that the fainter galaxy in *Ks* is the brighter member of the pair in F390W. Our target is a well-defined disk; the companion galaxy is much redder, and its spectroscopic redshift has not been measured. The NIRC2 image also resolved J142815+585442 into

two galaxies. We have no high-resolution color data in this case, and we define the target galaxy as the brighter member of the pair. We did not detect Mg II absorption associated with the third close pair, J143512+360424.

We defined a grid of rotation curves over a range of asymptotic velocities  $V_c$  and turnover radii,  $R_{RC}$ , using the following parametric model:

$$V_c(R) = (2/\pi)V_{rot} \arctan(R/R_{RC}). \quad (1)$$

For each target galaxy, we computed the projected velocities along the slit. We convolved these position – velocity curves with a model point spread function (psf) and compared the result to our H $\alpha$  position – velocity measurements. We minimized the fit residual to estimate the fitted asymptotic rotation speed,  $V_{rot}$ , and turnover radius,  $R_{RC}$ , for each galaxy in Table 2. We did not measure rotation curves J142815+585422 and J154956+070056 because of the small separation between the paired galaxies.

#### 2.4. Galaxy Environment

Determining the environments of our target galaxies would require extensive wide-field spectroscopy. We flag potential group members here using SDSS photometric redshifts which are not precise enough to establish group membership. A subset of these group candidates were spectroscopically observed as filler galaxies on the LRIS masks.

##### 2.4.1. Compact Groups

Heavy elements have been shown to be more widely dispersed around group members than isolated galaxies (Bordoloi et al. 2011; Johnson et al. 2015; Nielsen et al. 2018). The groups in these studies span a large range in mass and size. We will use the term *compact group* member to identify target galaxies that may have another luminous galaxy nearby, specifically within one virial radius in projection on the sky. Sightlines intersecting compact groups could show metal-line components from both halos, the blended systems producing stronger than average absorption strength.

Using the same definition of a compact group, Ho et al. (2017) identified four major axis targets as potential group members: J084725+254104, J091954+291345, J102907+421737, and J124601+173152. We measure a redshift  $z_{spec} = 0.18496$  for J102906.98+421733.3, leaving only J102909.45+421721.4 and our target J102907+421737 as a candidate group. We add six more potential group members – J081125+093616, J081708+091751, J092908+350942, J101713+183232, J104151+174603, and J154956+070044. The paired quasar spectra did not detect Mg II absorption near the redshift of two of these candidates.

The richest environment is likely that of J124601+173152. The environment of target J124601+173152 includes three brighter galaxies with consistent photometric redshifts, but our target is the closest the quasar sightline. Our target may be falling into the galaxy overdensity marked by J124559+173203 (40''4 W,  $\Delta V_{LOS} = 1010 \text{ km s}^{-1}$ ). Ho et al. (2017) flagged J124601+173152 because the host identification for the Mg II absorption in the J124601+173156 sightline was not unique.

We measure a spectroscopic redshift  $z = 0.19013$  for the filler galaxy J101712.54+183232.5, which is just  $119 \text{ km s}^{-1}$  redder than our target J101711.80+183237.6. The filler galaxy is closer to J101713+183232 sightline than our target but fainter.

Our target J104151.26+174558.7 lies just 4''7 from the J104151+174603 sightline, making it the most likely absorber host. It is possible, however, that a much more luminous galaxy, J104152.39+174520.2 which is 45''5 SE of the quasar, contributes to the absorption system; its redshift  $z_{spec} = 0.14189$  is  $112 \text{ km s}^{-1}$  bluer than our target's redshift.

The field surrounding galaxy J152027+421519 includes several objects whose photometric redshifts make them candidate group members. We measured a spectroscopic redshift  $z_{fill} = 0.29908$  for the nearest one, J152026.82+421529.4 (11''0 NW), eliminating it as the source of the Mg II absorption.

We conclude that most of the target galaxies do not belong to a compact group containing a galaxy more luminous than our target galaxy. The potential group members which we have flagged here identify sightlines where the environment might contribute to the absorption signature.

##### 2.4.2. Interacting Galaxies

Galaxy interactions may be integral to feeding gas to low redshift galactic disks. The galaxies identified above as potential group members may have interacted recently with another massive galaxy. Interactions with lower mass galaxies, including satellites, may also drive gas inflows. Here we identify morphological features that may mark disturbances caused by galaxy flybys or mergers.

We have already noted three examples of close pairs of galaxies. The  $K_s$  images in Figure 3a reveal smaller, fainter objects near our target galaxies. The potential companions with the two smallest separations are 6.8 kpc SE of J123049+071050 and 3.3 kpc E of J133740+055211. We looked for nearby galaxies that might drive the two-arm infrared spiral patterns and found several candidates. The spiral arms extending from J091954.11+291345.3, shown in Ho et al. (2019, in prep), may be driven by an interaction with J091954.44+291345.6 (red galaxy 4''4 E of our target) and/or J091954.07+291336.6 (red galaxy 8''7 SW). It is possible that our target J143603.16+375138.5 ( $z_{spec} = 0.31462$ ) recently interacted with J143603.11+375153.2 (14''7 N,  $z_{ph} = 0.36 \pm 0.06$ ) and/or J143601.36+375143.9 (21''9 NW,  $z_{ph} = 0.31 \pm 0.02$ ). The strongest absorber, J160951+353843 ( $W_r(\lambda) = 2.2\text{\AA}$ ), shows a disturbance towards the east; we did not find a brighter galaxy

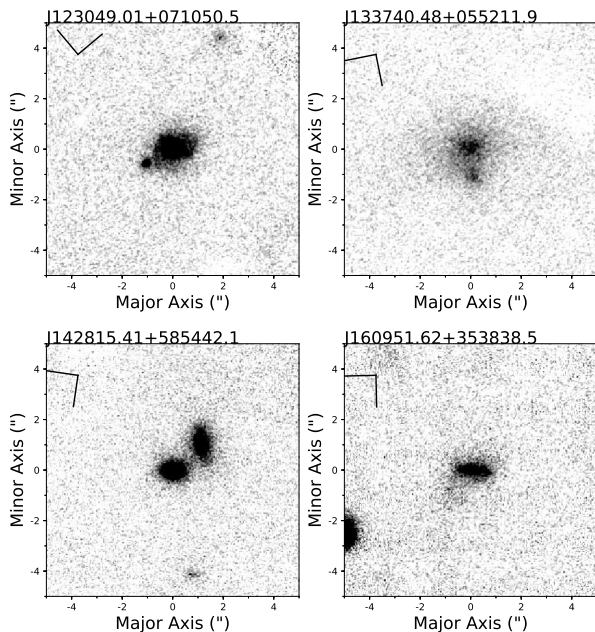


**Figure 3.** NIRC2/LGSAO  $K_s$ -band images. (a) Examples of targets showing signs of recent interactions. See Section 2.4.2 for description. (Figure 3b and 3c are available online and show images for other target galaxies.)

that could have interacted with the target, but an interaction with a less massive galaxy may explain the irregular morphology. One of the galaxies with spiral arms, J145844.18+170522.2, has no neighbors. Figures 3b and 3c show the NIRC2 images of the targets not shown elsewhere in the manuscript; note, however,

We adopt a specific SFR of  $1 \text{ Gyr}^{-1}$  as a definition for a recent starburst because it describes the dynamical timescale for galaxy – galaxy interactions. Our sample includes just four galaxies with specific SFRs above this threshold, but the images show morphological evidence for recent interactions in all of them. Two galaxies have specific SFR exceeding  $10^{-8} \text{ yr}^{-1}$ . One of these is the close pair J142815+585442; spatially resolved SEDs are needed to interpret the high specific SFR. The companion near J123049+071050 may have triggered the high specific SFR. The other galaxy with a similarly close companion, J133740+055211, has the third highest specific SFR in the sample. Our SED fitting is therefore consistent with the viewpoint that galaxy interactions are required to generate starbursts at redshift  $z \approx 0.2$ . The galaxy J150150+553227 also satisfies this starburst cri-

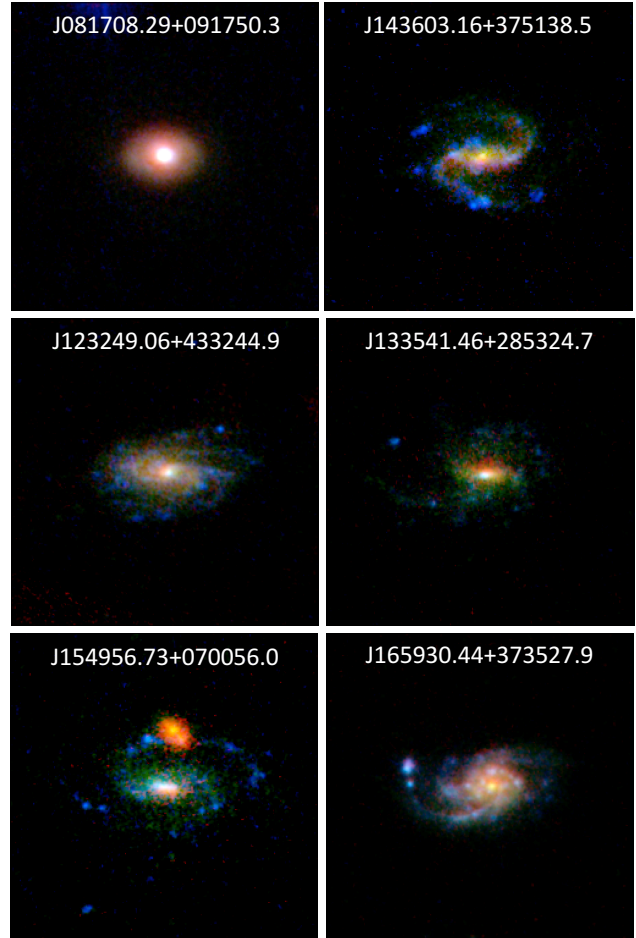


**Figure 4.** Composite F390W (blue), F814W (green), and  $K_s$  (red) images. The galaxies are ordered by specific SFR, increasing from left to right and from top to bottom. The cutouts are  $10''$  by  $10''$ .

terion.<sup>1</sup> The SDSS imaging indicates a more irregular morphology than is typical within our sample. We conclude that interactions with low mass galaxies are common among the targets with the highest specific SFRs, and we will discuss in Section 4 whether evidence for gas flows is more common in these systems.

Figure 4 shows composite images ordered by specific SFR. J081708+091750 is the only target in our sample that may have an active nucleus, which we identify based on the broad emission lines in our red LRIS spectrum. The imaging of J081708+091750 does not resolve spiral arms; the galaxy color is redder than most, and

<sup>1</sup> Its paired sightline is the only one among these four that did not detect Mg II absorption; see Section 2.5. No high-resolution images were obtained.

the specific SFR is low. The galaxy colors generally become bluer toward larger radii, something most easily seen in the J143603+375138 image and the star-forming member of J154956+070056 pair.

### 2.5. Quasar Sightlines & Absorber Properties

Measuring galaxy orientation on the sky allows us to describe the properties of the Mg II absorption relative to the projected plane of the galactic disk. Following the convention introduced in Bouché et al. (2012) (see their Figure 1), we define the *azimuthal angle* of a sightline as the angle  $\alpha$  between the galaxy major axis and a line drawn from the galaxy’s center to the quasar. By this definition,  $\alpha$  takes values from  $0^\circ$  to  $90^\circ$ ; Table 3 provides a second value that distinguishes among the four quadrants of the sky coordinates. We calculate the impact parameter of the sightline  $b$  from the angular separation of the pair defines and angular diameter distance at the galaxy redshift. Table 3 lists  $(b, \alpha)$  sky coordinates for the quasars relative to the target galaxy.

We continuum-normalized the quasar spectra and deredshifted each spectrum to the rest-frame of the target galaxy. We searched for Mg II absorption near the systemic velocity of the target galaxy. The doublet spacing robustly identified Mg II systems.<sup>2</sup> We measured the absorption strength and Doppler shift of each transition using custom software. We defined the integration limits by the intersection of the spectrum (plus one-sigma errorbars) with the continuum level. If this bandpass was narrower than the resolution element, then the latter was adopted allowing us to compute limits on non-detections. We integrated the total equivalent width,  $W_r$ , and calculated the equivalent-width-weighted mean velocity,  $\langle V(MgII) \rangle$ . We repeated this procedure 1000 times, perturbing the flux in each pixel by a random deviate scaled by the uncertainty. The median values and the one-sigma uncertainties computed from the resulting histograms define the measured values. Table 3 summarizes these absorption properties.

We detect Mg II absorption near the redshift of the target galaxy in 33 of the 50 sightlines. The median equivalent width is  $W_r(\lambda) = 0.31 \text{ \AA}$ . The optical depth at line center would be saturated for a single, thermal ( $10^4 \text{ K}$ ) component of this strength, so the optically thin limit gives only a lower limit on the column density  $N(\text{Mg II}) > 7.3 \times 10^{12} \text{ cm}^{-2}$ .

Figure 5 shows the line profiles. The Mg II  $\lambda 2796$  line is always noticeably stronger than the  $\lambda 2801$  line, so the Mg II  $\lambda 2803$  transition is not completely saturated in

these data. Only the weakest systems, however, have doublet ratios consistent with the 2:1 ratio of the optically thin limit. Some components of these systems must have optically thick Mg II  $\lambda 2796$ . Their absorption troughs are not black (zero intensity) because the spectral line-spread function smooths individual components and blends velocity components together.

In Figure 6 we plot the radial distribution of the rest-frame equivalent width of the Mg II  $\lambda 2796$  line as a function of impact parameter. The absorption strength declines as the separation of the sightline from the target galaxy increases, conforming to the previously established correlation between these quantities (Chen et al. 2010; Nielsen et al. 2013). Scaling the impact parameter to the virial radius (Churchill et al. 2013a,b) or halo scale radius produced similar results. This  $W - b$  relation defines the expected value of  $\langle W(b) \rangle$  in each sightline, and we define the excess equivalent width by  $\Delta W(\lambda 2796) \equiv W_r / \langle W(b) \rangle$ .

The 2-sigma upper limits for the non-detections have median value of  $0.1 \text{ \AA}$ . Most of the quasar spectra are therefore sensitive enough to detect a Mg II absorber of average strength out to  $b = 85 \text{ kpc}$ , as indicated by the solid line in Figure 6. The spectra without Mg II detections are generally sensitive enough to exclude typical absorption strengths; the upper limits are below  $\langle W(b) \rangle$ . Figure 6 shows four exceptions at large impact parameter: J081521+082623, J135522+303324, J171220+291806, and J114927+142002. Most of the non-detections do not exclude a Mg II system a standard deviation weaker than the median strength.

The transition from the ground state of Mg I to the  $3s3p \ ^1P_0$  level has a large oscillator strength,  $f = 1.83$  (Morton 2003). Neutral magnesium produces absorption at  $\lambda 2852.9642(1 + z_{abs})$ , a wavelength covered by our spectra for 48 of 50 sightlines.<sup>3</sup> We detect Mg I absorption in 12 sightlines. We find that the Mg I Doppler shifts are consistent with the Mg II Doppler shifts. Table 4 lists absorber equivalent widths. The line centers are optically thick, and these measurements place lower limits on the column density  $N(\text{Mg I}) \geq 7.59 \times 10^{12} \text{ cm}^{-2} W(\text{\AA})$ .

The ionization potential of Mg I is 7.65 eV, substantially lower than that of hydrogen. The detection of Mg I does not require the system to have a large neutral hydrogen column. The  $N(\text{Mg I})/N(\text{Mg II})$  ratio is sensitive to the total hydrogen density. The calculations in Figure 6 of Ellison et al. (2003) illustrate this point for a  $\log N(\text{HI}) = 19 \text{ cm}^{-2}$  slab of CGM photoionized

<sup>2</sup> The J142816+585432 spectrum cuts off between the 2796 and 2803 lines; detections of the Fe II 2586, 2600 determine  $z_{abs}$ .

<sup>3</sup> The Mg I line is not covered by our J142816+585432 and J123049+071036 spectra.

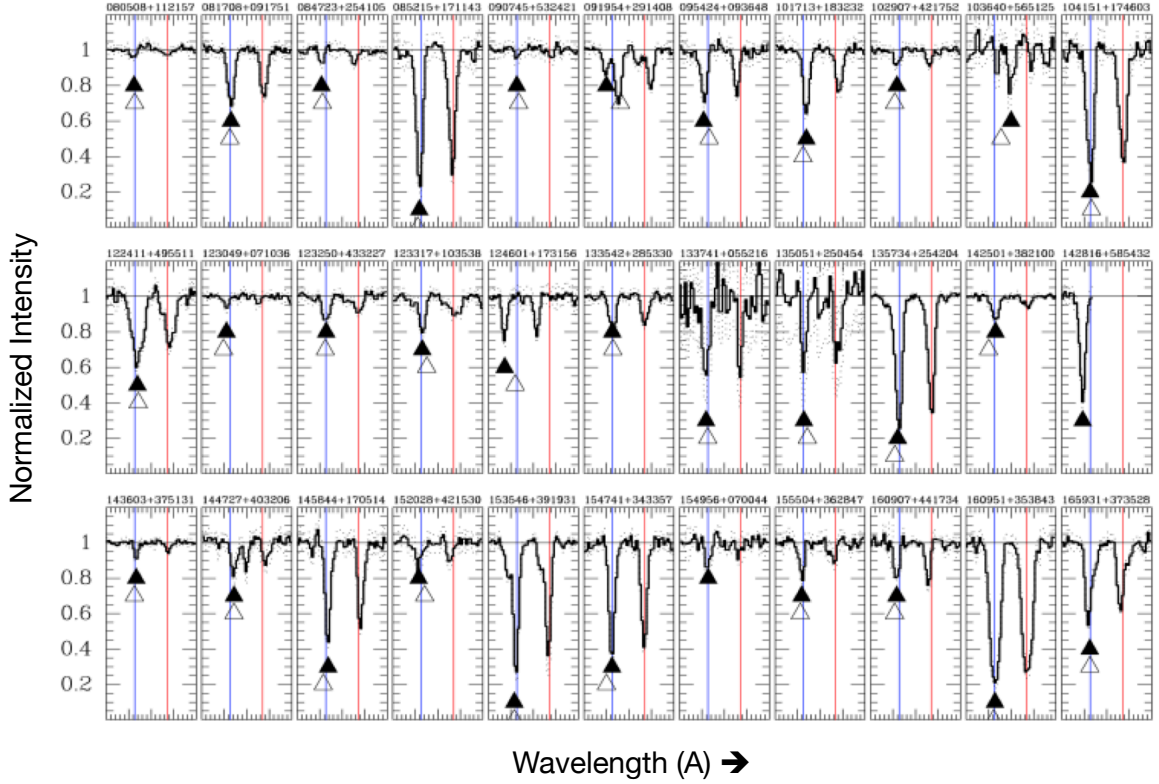


**Figure 5.** Continuum normalized quasar spectra showing Mg II system near the target galaxy redshift. Each spectrum has been deredshifted based on the emission-line redshift of the target galaxy. The vertical blue and red lines mark the vacuum wavelengths for Mg II 2796.352, 2803.531, respectively; tick marks are separated by 1 Å. The equivalent-width-weighted velocity (solid triangles) is significantly Doppler shifted in 22 of these 33 detections. Open triangles mark the projected rotation speed of an extended galactic disk with a flat rotation curve. The dotted lines show the 1-sigma uncertainties on the normalized flux.

by the UV background. The  $N(\text{MgI})/N(\text{MgII})$  ratio will be very low, less than a part per million for clouds at the average density of the CGM, which is between  $n_H \approx 1.5 - 4.0 \times 10^{-4} \text{ cm}^{-3}$  in the inner CGM (Werk et al. 2014). High gas density, roughly  $10 \text{ cm}^{-3}$  for  $\log N(\text{HI}) = 19 \text{ cm}^{-2}$ , raises the  $N(\text{MgI})/N(\text{MgII})$  ratio to 1%.

Sightlines with Mg I detections are not expected to select the large neutral hydrogen columns associated with galactic disks. Indeed damping wings on the hydrogen absorption-line profiles identify systems with  $N(\text{HI}) \geq 2 \times 10^{20} \text{ cm}^{-2}$ , and these damped Ly $\alpha$  absorbers (DLAs) are not typically detected in Mg I absorption (Rao & Turnshek 2000). Under the assumption that all our sightlines probe typical halo hydrogen columns,  $\geq 10^{14} \text{ cm}^{-2}$  (Chen et al. 2005), then the Mg I detections identify clouds of higher than average density and low ionization parameter.

We find the strongest Mg I system,  $W_{r,2853} = 1.64 \text{ \AA}$ , in the J104151+174603 sightline. The J104151+174558

Mg I absorption is about four times stronger than the second ranked system, suggesting this sightline has some unique attribute. The target galaxy is a confirmed group member, but it is not clear whether the environment explains the strong absorption. This galaxy also has the lowest stellar mass in our sample. The quasar sightline intersects the disk plane of at a radius of just  $R = 25.5 \text{ kpc}$ , and we note that six of the 12 sightlines with Mg I detections intersect the disk plane at  $R \leq 40 \text{ kpc}$ . Extended disks with hydrogen columns lower than DLAs could also produce some, but not all, of the Mg I systems.

In Section 2.4, we identified J091954+291345 as interacting with another galaxy. The widely separated Mg II components may come from separate galaxies. The J091954+291508 spectrum detects both velocity components in Mg I. We will argue in Section 4.2.2 that dense gas in galactic outflows provides another source of Mg I absorption.

Table 3. Summary of Sightlines

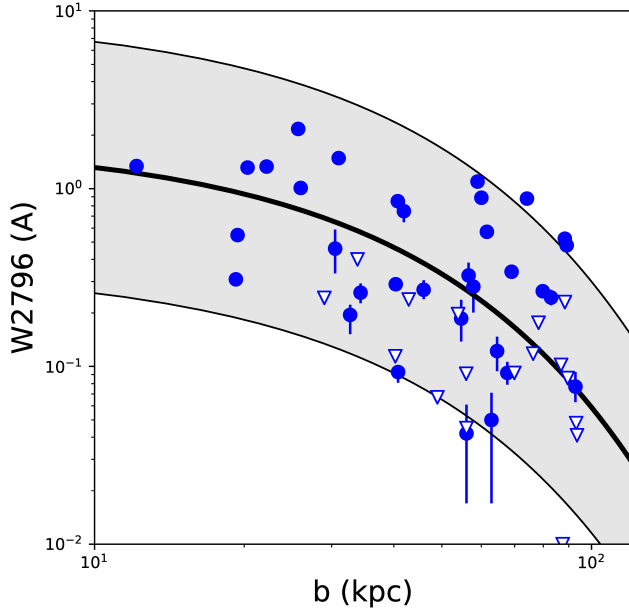
Quasar	RA (J2000)	DEC (J2000)	Target Galaxy	$\alpha$ ( $^{\circ}$ )	b (kpc)	$W_r^{2796}$ ( $\text{\AA}$ )	$W_r^{2803}$ ( $\text{\AA}$ )	$\langle W(b) \rangle$ ( $\text{\AA}$ )	$\langle V \rangle_{W}^{2796}$ ( $\text{km s}^{-1}$ )	$[V_{min}, V_{max}]$ ( $\text{km s}^{-1}$ )	$R_{resel}$ ( $\text{km s}^{-1}$ )
(1)	(2)	(3)	(4)	(5)	(6)	(7)	(8)	(9)	(10)	(11)	(12)
J080508.50+112157.2	08:05:08.50	+11:21:57.21	J080507.60+112208.3	82.3 (97.7)	62.9	$0.050_{-0.033}^{+0.021}$	$0.046_{-0.012}^{+0.015}$	0.212	$-17_{-30}^{+31}$	[-102, 71]	165
J081125.55+093626.2	08:11:25.55	+09:36:26.27	J081125.76+093616.9	64.7	33.81	$\leq 0.400$	$\leq 0.089$	0.579	...	...	160
J081521.64+082623.9	08:15:21.64	+08:26:23.95	J081521.69+082602.1	80.6	88.37	$\leq 0.230$	$\leq 0.742$	0.0880	...	...	165
J081708.71+091751.4	08:17:08.71	+09:17:51.49	J081708.29+091750.3	71.6 (108.4)	19.4	$0.548_{-0.024}^{+0.026}$	$0.444_{-0.023}^{+0.025}$	0.953	$16_{-6}^{+5}$	[-134, 176]	165
J084235.00+565350.2	08:42:35.00	+56:53:50.24	J084235.98+565358.7	3.5	42.87	$\leq 0.238$	$\leq 0.197$	0.424	...	...	105
J084723.56+254105.4	08:47:23.56	+25:41:05.40	J084725.06+254104.7	18.2 (161.8)	67.7	$0.092_{-0.013}^{+0.014}$	$0.111_{-0.020}^{+0.022}$	0.180	$-105_{-9}^{+9}$	[-176, -44]	105
J085215.34+171143.8	08:52:15.34	+17:11:43.85	J085215.36+171137.0	22.8 (157.2)	20.32	$1.314_{-0.043}^{+0.047}$	$1.190_{-0.046}^{+0.054}$	0.923	$-49_{-5}^{+5}$	[-225, 86]	165
J090745.28+532421.4	09:07:45.28	+53:24:21.47	J090743.44+532427.2	58.2 (-58.2)	56.03	$0.042_{-0.025}^{+0.019}$	$0.044_{-0.025}^{+0.020}$	0.269	$-6_{-15}^{+20}$	[-50, 42]	105
J091954.28+291408.3	09:19:54.28	+29:14:08.36	J091954.11+291345.3	15.3 (15.3)	88.36	$0.216_{-0.013}^{+0.014}$	$0.159_{-0.029}^{+0.019}$	0.088	$-147_{-7}^{+5}$	[-266, -8]	105
J092907.44+350942.0	09:29:07.44	+35:09:42.06	J092908.86+350942.2	71.4	88.36	$0.523_{-0.002}^{+0.018}$	$0.345_{-0.029}^{+0.018}$	0.088	$131_{-4}^{+5}$	[-51, 292]	165
J095424.10+093648.3	09:54:24.10	+09:36:48.33	J095423.27+093711.0	75.5 (-75.5)	56.02	$\leq 0.045$	$\leq 0.082$	0.269	...	...	165
J101713.07+183232.2	10:17:13.07	+18:32:32.24	J101711.80+183237.6	53.4 (126.6)	89.12	$0.480_{-0.025}^{+0.021}$	$0.333_{-0.040}^{+0.030}$	0.086	$-106_{-4}^{+4}$	[-284, 20]	160
J102907.73+421752.9	10:29:07.73	+42:17:52.93	J102907.56+421737.6	19.1 (160.9)	61.58	$0.572_{-0.033}^{+0.035}$	$0.401_{-0.035}^{+0.037}$	0.222	$65_{-8}^{+6}$	[-93, 219]	105
J103640.74+565125.9	10:36:40.74	+56:51:25.98	J103643.44+565119.0	21.4 (21.4)	64.56	$0.122_{-0.028}^{+0.025}$	$0.123_{-0.017}^{+0.019}$	0.200	$-53_{-20}^{+17}$	[-134, 34]	105
J104151.33+174603.4	10:41:51.33	+17:46:03.40	J104151.26+174558.7	29.8 (29.8)	57.84	$0.281_{-0.08}^{+0.06}$	$0.088_{-0.043}^{+0.048}$	0.253	$392_{-22}^{+16}$	[284, 516]	105
J104244.23+164656.1	10:42:44.23	+16:46:56.14	J104242.75+164638.4	88.0	12.15	$1.340_{-0.035}^{+0.036}$	$1.268_{-0.031}^{+0.046}$	1.224	$0_{-3}^{+3}$	[-174, 145]	165
J111239.11+353928.2	11:12:39.11	+35:39:28.20	J111238.15+353920.4	78.5	93.12	$\leq 0.048$	$\leq 0.019$	0.075	...	...	160
J113235.64+340428.3	11:32:35.64	+34:04:28.36	J113236.10+340453.0	80.9	55.95	$\leq 0.091$	$\leq 0.019$	0.270	...	...	165
J114334.84+284511.6	11:43:34.84	+28:45:11.67	J114335.30+284532.0	82.2	93.49	$\leq 0.041$	$\leq 0.075$	0.0737	...	...	160
J114927.97+142002.2	11:49:27.97	+14:20:02.27	J114926.83+142020.3	78.8	53.89	$\leq 0.197$	$\leq 0.224$	0.290	...	...	160
J122411.69+495511.1	12:24:11.69	+49:55:11.15	J122413.10+495515.4	45.6 (45.6)	89.51	$\leq 0.086$	$\leq 0.021$	0.0846	...	...	160
J123049.67+071036.9	12:30:49.67	+07:10:36.97	J123049.01+071050.5	4.0 (-176.0)	58.97	$1.096_{-0.034}^{+0.034}$	$0.721_{-0.031}^{+0.031}$	0.243	$64_{-6}^{+6}$	[-196, 306]	165
J123250.30+433227.3	12:32:50.30	+43:32:27.38	J123249.06+433244.9	79.0 (101.0)	97.73	$0.077_{-0.014}^{+0.016}$	$0.047_{-0.012}^{+0.012}$	0.075	$-93_{-17}^{+12}$	[-172, -21]	105
J123317.75+103538.1	12:33:17.75	+10:35:38.19	J123318.80+103542.1	3.9 (-3.9)	79.77	$0.265_{-0.022}^{+0.02}$	$0.180_{-0.025}^{+0.033}$	0.118	$6_{-8}^{+8}$	[-152, 151]	165
J124601.81+173156.4	12:46:01.81	+17:31:56.45	J124601.75+173152.1	10.8 (-169.2)	56.58	$0.325_{-0.022}^{+0.059}$	$0.302_{-0.039}^{+0.047}$	0.264	$20_{-29}^{+8}$	[-86, 129]	165
J133542.57+285330.4	13:35:42.57	+28:53:30.48	J133541.46+285324.7	76.3 (76.3)	19.25	$0.309_{-0.027}^{+0.026}$	$0.270_{-0.029}^{+0.031}$	0.958	$-293_{-8}^{+9}$	[-404, -200]	165
J133741.39+055216.9	13:37:41.39	+05:52:16.90	J133740.48+055211.9	81.3 (-98.7)	69.05	$0.341_{-0.018}^{+0.018}$	$0.268_{-0.019}^{+0.020}$	0.171	$-5_{-6}^{+7}$	[-155, 133]	165
J135051.46+250454.8	13:50:51.46	+25:04:54.85	J135051.70+250506.5	37.5 (37.5)	41.92	$0.747_{-0.1}^{+0.107}$	$0.510_{-0.112}^{+0.097}$	0.438	$-47_{-15}^{+10}$	[-155, 70]	160
					30.49	$0.460_{-0.126}^{+0.129}$	$0.501_{-0.199}^{+0.177}$	0.650	$8_{-20}^{+17}$	[-78, 60]	105

Table 3 continued

Table 3 (continued)

Quasar	RA (J2000)	DEC (J2000)	Target Galaxy	$\alpha$ ( $^{\circ}$ )	b (kpc)	$W_r^{2796}$ ( $\text{\AA}$ )	$W_r^{2803}$ ( $\text{\AA}$ )	$(W(b))$ ( $\text{\AA}$ )	$\langle V \rangle_W^{2796}$ ( $\text{km s}^{-1}$ )	$[V_{min}, V_{max}]$ ( $\text{km s}^{-1}$ )	$R_{resel}$ ( $\text{km s}^{-1}$ )
(1)	(2)	(3)	(4)	(5)	(6)	(7)	(8)	(9)	(10)	(11)	(12)
J135522.89+303324.7	13:55:22.89	+30:33:24.76	J135521.20+303320.4	1.6	78.22	$\leq 0.176$	$\leq 0.108$	0.125	...	...	165
J135734.41+254204.6	13:57:34.41	+25:42:04.62	J135733.86+254205.1	12.1 (-167.9)	30.99	$1.485^{+0.019}_{-0.018}$	$1.168^{+0.013}_{-0.013}$	0.638	$-33^{+3}_{-3}$	[-423, 197]	165
J140852.98+245631.4	14:08:52.98	+24:56:31.45	J140852.40+245637.3	65.2	29.00	$\leq 0.243$	$\leq 0.392$	0.684	...	...	160
J142501.46+382100.5	14:25:01.46	+38:21:00.52	J142459.82+382113.3	7.8 (172.2)	82.92	$0.244^{+0.026}_{-0.023}$	$0.117^{+0.009}_{-0.01}$	0.106	$21^{+12}_{-14}$	[-128, 221]	165
J142816.69+585432.6	14:28:16.69	+58:54:32.62	J142815.41+585442.1	53.3	72.39	$0.879^{+0.034}_{-0.029}$	...	0.144	$-180^{+4}_{-5}$	[-316, -15]	165
J142911.26+324824.0	14:29:11.26	+32:48:24.03	J142910.91+324840.2	67.8	69.94	$\leq 0.092$	$\leq 0.138$	0.166	...	...	160
J143511.53+360437.2	14:35:11.53	+36:04:37.22	J143512.93+360424.9	48.7	87.22	$\leq 0.010$	$\leq 0.058$	0.0906	...	...	105
J143603.56+375131.3	14:36:03.56	+37:51:31.37	J143603.16+375138.5	86.5 (-93.5)	40.81	$0.093^{+0.009}_{-0.012}$	$0.066^{+0.010}_{-0.010}$	0.455	$35^{+4}_{-10}$	[-46, 113]	105
J144727.50+403206.3	14:47:27.50	+40:32:06.34	J144727.42+403217.8	41.5 (41.5)	45.94	$0.270^{+0.035}_{-0.031}$	$0.168^{+0.036}_{-0.026}$	0.381	$89^{+12}_{-12}$	[-34, 221]	165
J145844.76+170514.7	14:58:44.76	+17:05:14.79	J145844.18+170522.2	56.6 (123.4)	40.75	$0.850^{+0.032}_{-0.029}$	$0.722^{+0.030}_{-0.028}$	0.456	$55^{+5}_{-5}$	[-89, 253]	105
J150118.32+155623.0	15:01:18.32	+15:56:23.04	J150119.24+155602.2	57.6	76.29	$\leq 0.118$	$\leq 0.260$	0.134	...	...	165
J150150.93+553241.1	15:01:50.93	+55:32:41.19	J150150.28+553227.5	89.2	40.29	$\leq 0.114$	$\leq 0.118$	0.463	...	...	165
J152028.18+421530.3	15:20:28.18	+42:15:30.32	J152027.21+421519.3	48.9 (-48.9)	54.67	$0.186^{+0.051}_{-0.048}$	$0.136^{+0.036}_{-0.035}$	0.282	$-65^{+29}_{-23}$	[-146, 26]	105
J153546.29+391931.1	15:35:46.29	+39:19:31.18	J153546.74+391932.2	57.2 (-122.8)	22.19	$1.331^{+0.023}_{-0.022}$	$1.074^{+0.040}_{-0.040}$	0.865	$-64^{+3}_{-2}$	[-403, 136]	105
J154453.86+165710.1	15:44:53.86	+16:57:10.11	J154454.75+165703.7	47.1	48.96	$\leq 0.067$	$\leq 0.057$	0.343	...	...	105
J154741.88+343357.3	15:47:41.88	+34:33:57.32	J154741.46+343350.8	4.0 (-176.0)	25.99	$1.009^{+0.023}_{-0.025}$	$0.898^{+0.028}_{-0.030}$	0.759	$-12^{+3}_{-3}$	[-152, 156]	165
J154956.87+070044.9	15:49:56.87	+07:00:44.93	J154956.73+070056.0	85.4 (-85.4)	32.68	$0.195^{+0.027}_{-0.043}$	$0.080^{+0.035}_{-0.032}$	0.602	$5^{+8}_{-15}$	[-76, 103]	160
J155504.39+362847.9	15:55:04.39	+36:28:47.96	J155505.27+362848.4	44.6 (135.4)	34.30	$0.260^{+0.033}_{-0.033}$	$0.151^{+0.050}_{-0.047}$	0.570	$-45^{+11}_{-12}$	[-176, 43]	105
J160907.45+441734.4	16:09:07.45	+44:17:34.43	J160906.72+441721.5	7.3 (172.7)	40.37	$0.290^{+0.023}_{-0.02}$	$0.299^{+0.026}_{-0.023}$	0.462	$-59^{+5}_{-6}$	[-151, 30]	105
J160951.81+353843.7	16:09:51.81	+35:38:43.78	J160951.62+353838.5	25.5 (-154.5)	25.69	$2.167^{+0.035}_{-0.033}$	$2.065^{+0.053}_{-0.040}$	0.767	$6^{+2}_{-3}$	[-213, 231]	165
J165931.92+373528.8	16:59:31.92	+37:35:28.80	J165930.44+373527.9	84.6 (95.37)	60.03	$0.889^{+0.028}_{-0.024}$	$0.769^{+0.024}_{-0.023}$	0.234	$-10^{+5}_{-5}$	[-158, 233]	160
J171220.81+291806.9	17:12:20.81	+29:18:06.96	J171222.58+291758.6	35.9	86.83	$\leq 0.102$	$\leq 0.010$	0.0928	...	...	165

NOTE— Column Descriptions: (1) Quasar name. (2,3) Quasar coordinates. (4) Target Galaxy. (5) Azimuthal angle between the galaxy – quasar position angle and the galaxy major axis. We define  $\alpha$  on the interval  $[0^{\circ}, 90^{\circ}]$  when we stack the sightlines on a single quadrant of the sky coordinates. When we need to distinguish among the four quadrants, we define azimuthal angle relative to the receding side of the major axis on the interval  $-180^{\circ} < \alpha \leq 180^{\circ}$  such that positive values are consistent with positive z-values as defined in Section 4.1. (6) Projected distance of the quasar sightline from the target galaxy. (7) Rest-frame equivalent width of Mg II  $\lambda 2796$ ; the  $2\sigma$  upper limit is listed for non-detections. (8) Rest-frame equivalent width of Mg II  $\lambda 2803$ ; the  $2\sigma$  upper limit is listed for non-detections. (9) Predicted equivalent width. We adopt the fitted  $W_r - -b$  relation from (Nielsen et al. 2013). (10) Equivalent-width-weighted Doppler shift of the Mg II  $\lambda 2796$  line, measured relative to the target galaxy redshift. (11) Velocity range of the absorption system, not corrected for the instrumental profile. (12) Velocity resolution (full width at half maximum intensity).



**Figure 6.** Rest-frame equivalent width of Mg II 2796 versus impact parameter. Absorption strength declines with the distance of the sightline from the galaxy, consistent with previous studies. For comparison, the black line shows the maximum likelihood fit from Nielsen et al. (2013); the shaded region shows the root-mean-square variation between this fit and their sample.

**Table 4.** Mg I Detections

Quasar	$W_r(MgI)$ (Å)	$W_r(MgI)/$ $W_r(MgII)$
J104151.33+174603.428	$1.64 \pm 0.05$	1.2
J160951.81+353843.728	$0.38 \pm 0.03$	0.18
J085215.34+171143.828	$0.29 \pm 0.03$	0.22
J153546.29+391931.128	$0.26 \pm 0.01$	0.20
J135734.41+254204.628	$0.25 \pm 0.01$	0.17
J154741.88+343357.328	$0.15 \pm 0.02$	0.15
J165931.92+373528.828	$0.12 \pm 0.02$	0.13
J160907.45+441734.428	$0.11 \pm 0.02$	0.38
J145844.76+170514.728	$0.10 \pm 0.02$	0.12
J091954.28+291408.328	$0.093 \pm 0.012$	0.18
J124601.81+173156.428	$0.070 \pm 0.016$	0.23
J122411.69+495511.128	$0.049 \pm 0.015$	0.045

NOTE— *Col 1.* Quasar sightline. *Col 2.* Rest-frame Equivalent width of Mg I  $\lambda 2853$  absorption near the redshift of the target galaxy. *Col 3.* Equivalent width ratio of rest-frame Mg I  $\lambda 2853$  to Mg II  $\lambda 2796$ .

### 3. KINEMATICS OF LOW-IONIZATION CIRCUMGALACTIC GAS

Figure 5 shows the Mg II line profiles in the reference frames of the target galaxies. Asymmetric profiles are common, indicating that multiple velocity components contribute to the absorption systems. Blending of unresolved components can produce larger equivalent widths than a single saturated component. Furthermore, because the resolution does not resolve saturated components, line strengths only place lower limits on the  $Mg^+$  column density. For these reasons, we describe each absorption system by its equivalent-width-weighted mean velocity,  $\langle V(MgII) \rangle$ , and the rest-frame equivalent width of Mg II  $\lambda 2796$ ,  $W_r$ .

The components contributing to an absorption system may include a warped disk, streams produced by the tidal disruption of satellites, or a galactic outflow. Cold flow accretion may also produce absorption, although calculations suggest these streams are more common at higher redshift. Numerous recent studies address the origin of cool circumgalactic gas (Voit et al. 2015; McCourt et al. 2015, 2016; Voit et al. 2017; Gronke & Oh 2018; Schneider et al. 2018), but no consensus regarding its formation and destruction has been reached. Observations of the circumgalactic gas kinematics offer a new perspective on these problems.

A unique aspect of our study is the large number of measured galactic rotation curves. We use them to illustrate the line-of-sight velocities produced by circular orbits in the plane of the galactic disk. These centrifugally supported disk components are indicated in Figure 5. Sec. 4 will discuss individual velocity components further. In this section, we describe the absorption systems.

#### 3.1. Corotation with Galactic Disks

We detected Mg II absorption in 33 sightlines and measured galactic rotation curves for 31 host galaxies. We compare  $\langle V(MgII) \rangle$  to the projected disk rotation speed. If the sign of the Mg II Doppler shift matches the sign of the disk rotation, then we say the system *corotates* with the disk. When the equivalent-width-weighted absorption cannot be distinguished from the systemic velocity of the galaxy, i.e., the Doppler shift is less than our measurement uncertainties, we label the system *systemic absorption*. *Counter-rotating* absorbers have a net Doppler shift, but the sign of the Doppler shift is opposite that of the galactic disk.

Figure 7 shows the locations of the quasar sightlines relative to the projection of the galactic disks on the sky. Each galaxy image has been rotated to align the semi-major axis with the abscissa. The location of the

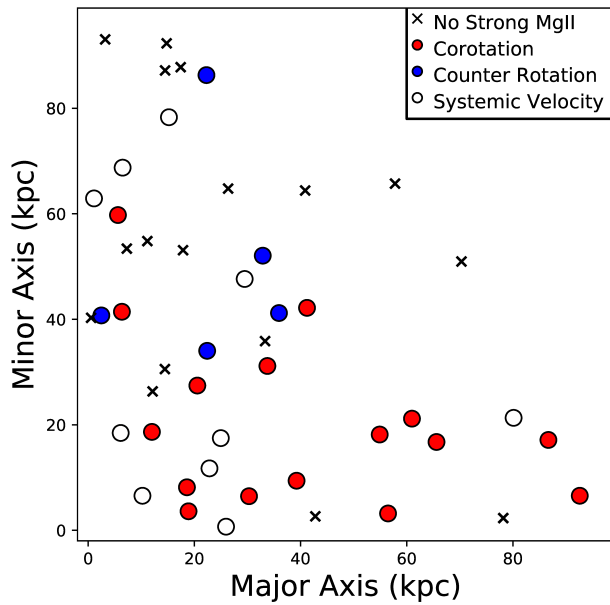


**Figure 7.** *Top:* Doppler shifts of Mg II systems in quasar sightlines. The location of each sightline is plotted relative to the projected plane of the galactic disk on the sky. The redshifted side of the major axis has been aligned with the positive x-axis of the coordinate system. The colorbar describes corotation (red), counter rotation (blue), and systemic absorption (white). Sightlines without Mg II detections are marked with an X.

sightline on the sky is given by the polar coordinates  $(b, \alpha)$ .

At azimuthal angles less than  $46^\circ$ , we find 12 corotating systems. Ten of these are within  $30^\circ$  of the major axis, and we described them previously in Ho et al. (2017). We add J122411+495511 ( $45.6^\circ$ ) and J144727+403206 ( $41.5^\circ$ ). Over the same range of azimuthal angle, the  $\langle V(MgII) \rangle$  measurements are indistinguishable from the systemic velocity along 5 additional sightlines. We find no counter-rotating absorbers. The absence of counter-rotating gas is highly significant.

To appreciate the significance of these statistics, consider tossing two coins. There are four possible outcomes, and two of these result in the coins showing the same face. This thought experiment is analogous to measuring whether the CGM and the galactic disk have an angular momentum component in the same direction. Out of 12 successful coin tosses (or net Doppler shift measurements), the chance of getting alignment all 12 times is  $P = 2.4 \times 10^{-4}$ . This result comes from a binomial distribution with a mean of 6 and standard deviation of 1.73.

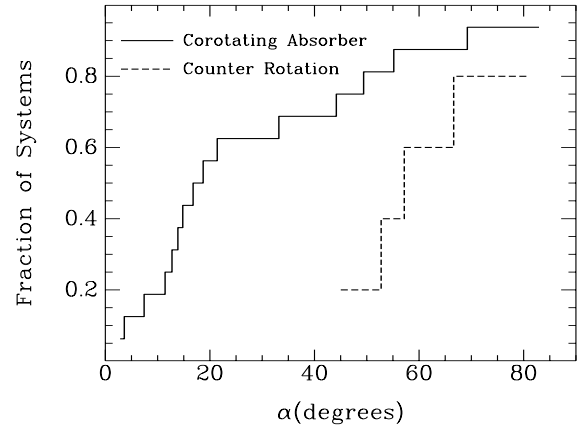


**Figure 8.** Cumulative azimuthal distributions of corotating and counter-rotating Mg II systems. To compare these distributions we use Kuiper’s statistic, a KS-test defined on a circle to eliminate sensitivity to the endpoints. The null hypothesis states that the sightlines with corotating systems are drawn from the same parent distribution as the sightlines with counter-rotating systems. The probability of the null hypothesis is 3.8%, so these distributions are significantly different. The systemic absorbers in contrast are randomly distributed in azimuthal angle as shown in Figure 7.

If we consider only those sightlines within  $45^\circ$  of the minor axis, then the number of counter-rotating Mg II systems is similar to the number of corotating systems. We find no correlation between the sign of the Doppler shift of the CGM and the rotation of galactic disks near the minor axis.

Figure 8 compares the azimuthal distribution of corotating and counter-rotating Mg II systems. A KS test quantifies the chance of finding such a large separation between two samples drawn from the same underlying distribution. We used Kuiper’s statistic to provide uniform sensitivity across azimuthal angle (Press et al. 1992) and found the probability of this null hypothesis is just 3.8%. The corotators and counter-rotators do not have the same azimuthal distribution.

Figure 9 shows how the cumulative distribution of Mg II detections and non-detections differ in azimuthal angle. The paucity of non-detections at low  $\alpha$  means the covering factor of strong Mg II absorption is high there. Three of the non-detections correspond to sightlines that probe the large open area in the upper right quadrant of Figure 7. The sensitivity limits for each sightline are provided in Table 3 and must be taken into account when using these data to measure covering fractions.

### 3.2. Velocity Range & Absorption Strength

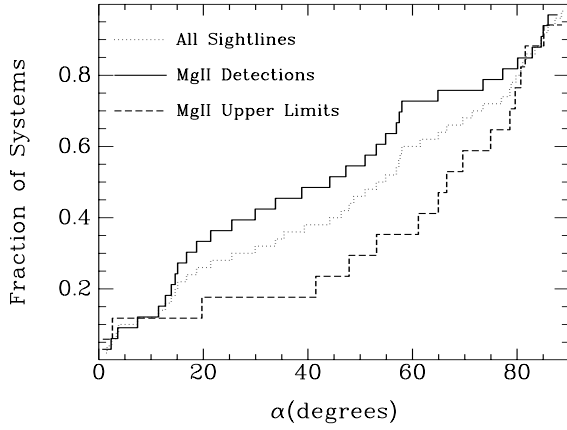


**Figure 9.** Cumulative azimuthal distribution of Mg II detections and non-detections. The probability that these samples were drawn from the same parent distribution is 7.3%, where we have again used the Kuiper statistic to perform the KS-test. Comparison to the distribution of all sightlines indicates that the difference is driven in large part by the small fraction of non-detections near the major axis.

We expect the line strength to be sensitive to the gas kinematics because of optical depth effects. In Figure 10 we show that the equivalent width correlates strongly with the velocity range of the Mg II absorption. A large velocity range for the absorption indicates a kinematic disturbance. Turbulent gas motion may broaden individual absorption components. The largest velocity ranges reach many hundred  $\text{km s}^{-1}$ , however, and are more likely produced by multiple velocity components.

For a given impact parameter then, absorption tends to be stronger than average along sightlines within  $45^\circ$  of the minor axis. We applied a KS test to the sightlines with an excess and a deficit of absorption. Kuiper’s statistic yields a 20% probability that the azimuthal distributions of excess and deficit absorbers were drawn from the same parent population.<sup>4</sup> The significance of the azimuthal variation of the excess absorption is therefore marginal in our sample. Other studies, however, robustly show that equivalent width increases toward the minor axis (Bordoloi et al. 2011; Lan & Mo 2018). Two factors explain the difference. First, our sample includes a larger fraction of low  $b$ , low  $\alpha$  sightlines; these major axis sightlines also show excess equivalent width, diluting the trend measured in the opposite direction at larger  $b$ . Second, studies like the one of Lan & Mo (2018) have many, many more sightlines. We conclude

<sup>4</sup> This analysis includes J142816+585432 and J154956+070044, the two galaxies without rotation curve measurements, even though they cannot be shown in Figure 13.

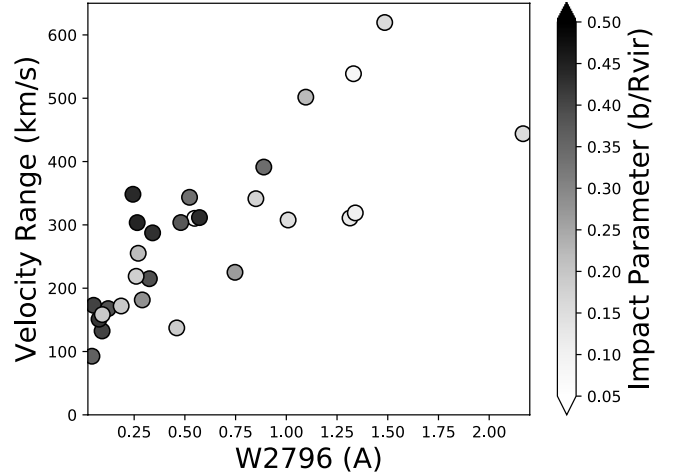


**Figure 10.** Velocity range of Mg II absorption versus rest-frame equivalent width of Mg II 2796. The grayscale identifies the impact parameter of each sightline. The Spearman rank-order correlation coefficient is  $r_s = 0.82$  ( $4.3\sigma$ ), indicating a significant correlation.

that there is strong azimuthal variation in excess equivalent width, which increases with azimuthal angle at  $b > 40$  kpc. For the first time, however, we demonstrate that equivalent widths actually increase toward the major axis at smaller impact parameters. Figure 11 bins our data by impact parameter and further illustrates these azimuthal variations.

To gain insight into the nature of the extra component, we examined how line strength depends on azimuthal angle. Figure 12 separates the sightlines into very strong, strong, and optically thin Mg II absorption. The strong systems confirm the previously established trend (Bordoloi et al. 2011; Bouché et al. 2012; Kacprzak et al. 2012; Lan et al. 2014; Lan & Mo 2018), namely that the equivalent width increases toward the minor axis. Previously missed, however, is the very strong absorption near the major axis at small impact parameter. The very strong absorption at  $b < 40$  kpc was missed by previous surveys due their small number of close pairs. One possible explanation for this very strong component is absorption by the galactic disks.

We detect optically thin systems at random locations in the  $(b, \alpha)$  projection. Their strength is not correlated with azimuthal angle. These weak lines directly measure the column density  $N(\text{Mg}^+)$ . We find no variation in  $N(\text{Mg}^+)$  column with azimuthal angle.

To gain more insight into which sightlines show excess absorption, we divide the rest-frame equivalent widths by the average value of the Nielsen et al. (2013) fit. The resulting ratio is used to scale the size of the points in Figure 13, which shows the sightline location rel-

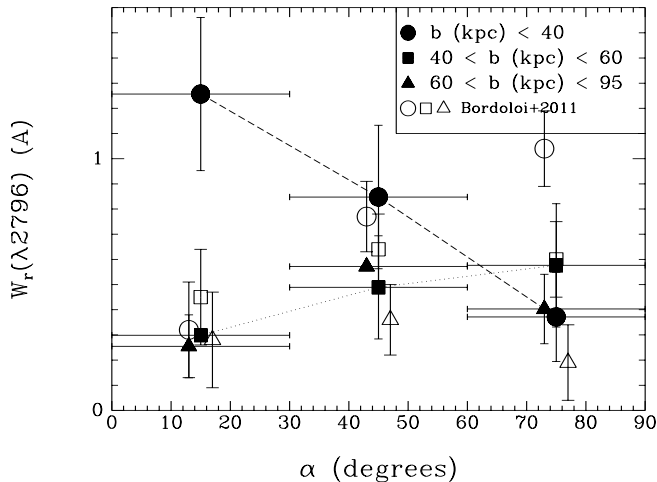


**Figure 11.** Absorption strength vs. azimuthal angle, binned by impact parameter. The minor-axis excess seen at  $b > 40$  kpc agrees with [Bordoloi et al. \(2011\)](#) and [Lan & Mo \(2018\)](#) who analyzed large numbers of sightlines. The absorption strength at low  $b$ , however, increases toward the major axis; previous studies did not sample the low  $b$  sightlines well.

ative to a coordinate system determined by the projected geometry of each galaxy. We find 14 systems with  $W_r/\langle W(b) \rangle > 1.5$ , and 10 of these have azimuthal angles  $\alpha > 45^\circ$ . The excess absorption,  $W_r/\langle W(b) \rangle$ , has a weak positive correlation with specific SFR. Note that the absorption strength,  $W_r$ , is not correlated with the galactic SFRs in our sample.

Do all the excess equivalent width systems have blended velocity components? Our sample includes five systems with  $W_r \geq 3\langle W(b) \rangle$ . Three of these systems – J091954+291408, J095424+093648, and J142816+585432 lie above the shaded region in Figure 6, and the other two systems J122411+495511 and J165931+373528 lie nearby. As shown above, two components produce the large excess equivalent width in J091954+291408. Line wings are prominent on the J095424+093648, J122411+495511, and J165931+373528 Mg II profiles. Strong excess absorption is therefore produced by blends of multiple components.

We previously showed that the stronger component in the J165931+373528 spectra can be easily described by a galactic outflow ([Kacprzak et al. 2014](#)). Like the J165931+373528 sightline, the J122411+495511 and J095424+093648 sightlines probe large azimuthal angles. We will discuss whether galactic outflow create their equivalent width excess.

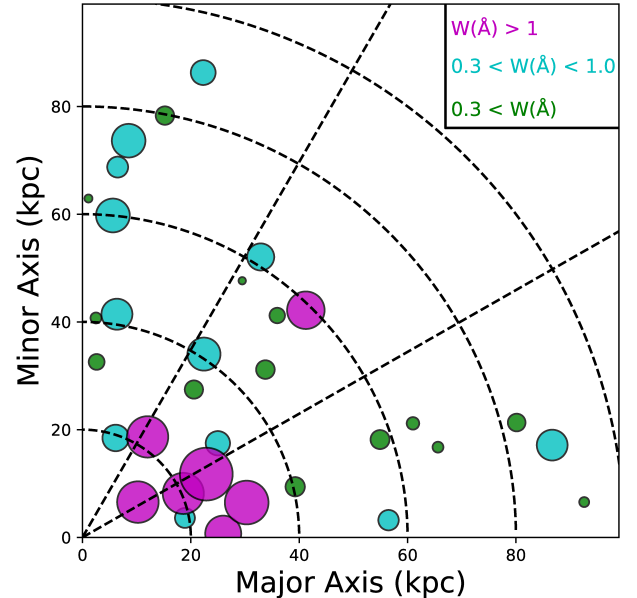


**Figure 12.** Absorption strength vs. azimuthal angle. We have scaled the symbol size by the equivalent width, illustrating the very strong absorbers ( $W_r \geq 1.0 \text{ \AA}$ ), strong absorbers ( $0.3 \leq W_r < 1.0 \text{ \AA}$ ), and optically thin absorbers ( $W_r < 0.3 \text{ \AA}$ ). Many of the very strong absorbers were found in low impact parameter sightlines near the major axis, so they may intersect extended disks. The strong absorbers confirm the established trend that absorption strength increases near the minor axis.

#### 4. DISCUSSION

We find that a high fraction of Mg II systems corotate with galactic disks, particularly in sightlines near the galactic major axis. This result rules out the simplest model for the CGM kinematics; the motion of the low-ionization gas is not random. Matched signs for the absorbers and disk Doppler shifts indicate the inner CGM has a component of angular momentum in the direction of the disk’s angular momentum vector. The high angular momentum of cold flow gas in simulations is related to the fact that it tends to be accreted along filaments ([Stewart et al. 2011b](#)). Those filaments also direct satellites toward the central galaxy, and the gas stripped from the satellite winds provides another important source of material for building galactic disks ([Anglés-Alcázar et al. 2017](#); [Hafen et al. 2018](#)). The detection of high angular momentum gas in the CGM raises the question of whether the warped extended disks that form in the simulations might be common even at low redshift. Direct 21-cm observations of disks on circumgalactic scales are rare ([Pisano 2014](#)) because they require detecting H I column densities well below the critical value where the

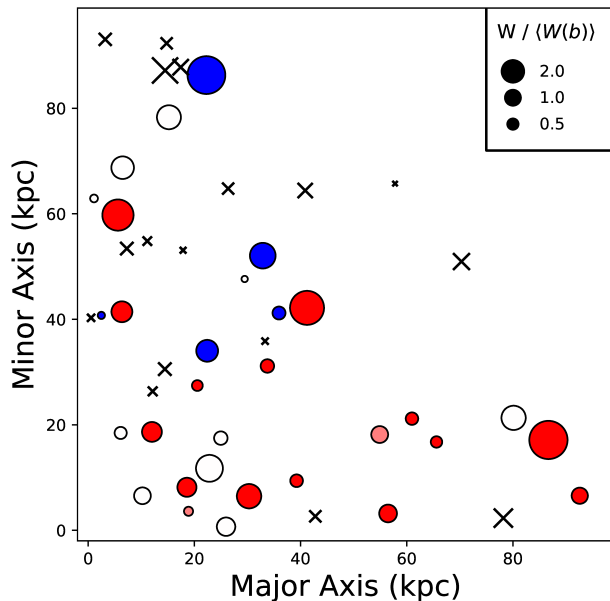


**Figure 13.** Relative Mg II absorption strength. The coordinate system is the same as in Figure 7. Large and small symbols indicate an excess or a deficit of absorption, respectively, compared to the average equivalent width at that impact parameter. The solid line in Figure 6 illustrates the factor  $\langle W(b) \rangle$  that we have used to remove the strong dependence of absorption strength on impact parameter. The largest excess occurs in J091954+291408. Typically, however, large excess equivalent width is found most often along sightlines with large azimuthal angles,  $\alpha > 45^\circ$ , and larger impact parameters,  $b > 40$  kpc.

neutral gas is vulnerable to the cosmic ionizing background (Bland-Hawthorn et al. 2017).

We also confirm the presence of a kinematic disturbance concentrated around the minor axis where no net corotation is measured. This result is consistent with the classical picture of a bipolar wind. Yet simulated outflows from disks in a cosmological setting, where the disk is free to wobble and move, sometimes produce more spherical outflows even at low redshift. The short lifetime of accelerated clouds raises concerns about interpreting the kinematic disturbance as a continuous outflow. What we observe might be better described as condensation triggered by a wind, a fine distinction that has important implications for modeling feedback.

To gain further insight into these outstanding issues, we compare the circumgalactic gas kinematics to two axisymmetric models in this section. Doing so requires an assumption about the location of the absorbing gas along each sightline, introducing potential systemic errors that do not affect the results of the previous sec-

tion. In Section 4.1 we compare the  $\langle V(\text{MgII}) \rangle$  measurements to an extended disk model in order to further evaluate the possibility that corotating gas feeds galactic disks. Minor-axis sightlines may miss extended disk-like structures because they intersect the disk plane at larger galactocentric radii than do major-axis sightlines at similar impact parameters on the sky. We resolve the orientations of galactic disks in Section 4.2 and test the conjecture that bipolar outflows produce the excess absorption at high azimuthal angles. After identifying outflow components and describing their relationship to galaxy properties, we return to our discussion of the disk plane in Section 4.3, where we place limits on the spatial extent of the corotating gas.

#### 4.1. Thin Disk Component

In this section we describe the velocity component added to an absorption system by a centrifugally supported disk. Thin disk models will not explain the velocity range of an entire Mg II system. A sightline intersects a thin disk over a short pathlength and samples a small range in line-of-sight velocity, producing a narrow line profile. The broader range observed may be attributed to spatially distinct components along a sightline, gas inflow within a disk (Ho et al. 2017), and/or a cylindrical model for the corotation (Steidel et al. 2002). Higher resolution spectroscopy would resolve distinct velocity components.<sup>5</sup> We evaluate which systems might include a component produced by a centrifugally supported gas near the disk plane.

For our purposes here, an extended disk is an axisymmetric structure with an angular momentum vector roughly parallel to that of the galactic gas disk. An extended disk has a finite radius. Sightlines that intersect the disk plane at small radii are more likely to detect an extended disk. All the major axis sightlines intercept the disk plane at  $R < 100$  kpc. A few minor-axis sightlines also pass through the disk plane at relatively small radii,  $R \lesssim 40$  kpc, but other high minor-axis sightlines intercept that plane at many hundred kpc. Disk inclination has a large effect on whether minor-axis sightlines intersect an extended disk. We project all the sightlines onto the disk plane for purposes of illustration because we do not know the size of these structure a priori.

Consider an extended thin disk whose angular momentum vector is parallel to that of the galactic disk. The disk lies in the xy-plane and has an angular momentum vector in the z-direction. We calculate the co-

<sup>5</sup> We detected two components from the CGM of J091954.11+291345.3, and in this section we consider only the stronger component.

ordinates  $(x_0, y_0, 0)$  where each sightline intersects the disk plane. In cylindrical polar coordinates the sightline intersects the disk at a point  $(R, \phi, 0)$ , where the angle  $\phi$  is measured from the x-axis to the point  $(x_0, y_0)$ . The inclination  $\iota$  describes the angle between the z-axis and the sightline, and we adopt the convention that  $\iota$  is positive (negative) for quasars at positive (negative) z-coordinates.

We choose the x-axis so that it is aligned with the receding semi-major axis of the disk on the sky. Then we have  $x_0 = b \cos \alpha$ , where the azimuthal angle  $\alpha$  is defined on the interval  $(-180^\circ, 180^\circ]$ . The value of  $y_0$  depends on the disk inclination as well as  $b \sin \alpha$ . We adopt the convention where the quasar is at some very large value of  $y$ , and the observer is at a very negative value of  $y$ . A positive inclination then produces  $y_0 = -b \sin(\alpha) / \cos(\iota)$ , and the sign is reversed for a negative disk inclination. The quasar sightline intersects the disk plane at radius

$$R = b \sqrt{1 + \sin^2 \alpha \tan^2 \iota}. \quad (2)$$

We project the rotation of the extended disk onto the plane of the sky. Disks produce absorption at a maximum Doppler shift,  $V_c(R) \sin \iota$ , in major axis sightlines. The same disks produce absorption at the systemic velocity in minor-axis sightlines because the velocities of the circular orbits are perpendicular to the sightline. Smaller Doppler shifts will be detected at intermediate azimuthal angles. The orbital motion produces a line-of-sight velocity

$$v_{los} = \frac{V_c(R) \sin \iota \cos \alpha}{\sqrt{1 + \sin^2 \alpha \tan^2 \iota}}. \quad (3)$$

in the quasar sightline. The major-axis sightlines therefore have a more favorable geometry for identifying a disk kinematically. Ambiguity about which side of the disk is nearer will not affect the predicted line-of-sight velocities for circular orbits.

Motivated by the correlation in the signs of the Doppler shifts of the Mg II systems and the disk model, we examined the relationship between the magnitude of  $\langle V(MgII) \rangle$  and the projected speed. Starting with the subset of sightlines at  $R \gtrsim 30$  kpc, we computed the Spearman rank order correlation coefficient, finding a positive correlation. We then increased the sample size by one sightline iteratively until all sightlines were included. The Spearman rank-order correlation coefficient increased up to  $R \leq 70$  kpc and then decreased sharply as we continued to add sightlines at  $R \geq 90$  kpc. This result suggests the extent of the corotating gas that is *disky* is roughly  $R_{max} \approx 80 \pm 10$  kpc. The lighter

colored points in Figure 14 illustrate this correlation between the Mg II Doppler shifts and the disk model.<sup>6</sup>

This result strongly suggests that centrifugal support of the low-ionization CGM is significant out to at least  $R_{max}$ . We observed very few major-axis sightlines at larger radii, so our results do not exclude corotating gas at  $R > R_{max}$ . Inspection of Figure 14 also shows that the correlated points at  $R < R_{max}$  generally have lower speeds than would be expected for circular orbits. Discrepancies introduced by the warping of large disks would scatter the residual velocities in both directions. The lower observed speeds indicate that the angular momentum of the low-ionization gas is not entirely sufficient to support it against gravity, so the gas spirals in toward the galaxy. We have simply extrapolated a flat rotation curve to make this comparison because it makes our results easier to reproduce. Halo circular velocities, see Section 4.1 and Figures 6 and 7 of Ho et al. (2017), are lower than this extrapolation predicts but still higher than the deprojected  $\langle V(MgII) \rangle$  values.

Sightlines that do not detect Mg II place limits on the shape of the corotating structure. Extended disks, for example, are axisymmetric by definition, and sightlines intersecting the disk plane at any coordinates  $(R, \phi)$  will detect absorption so long as  $R$  is less than the maximum extent of the disk. In Figure 15 the covering fraction of Mg II detections is near unity out to  $R \approx 70$  kpc, a radius consistent with the value of  $R_{max}$  estimated above from the velocity correlation. We estimate that the typical galaxy in our sample may be surrounded by a gaseous disk-like structure which extends to  $\approx 70 - 80$  kpc.

Absorption strengths provide further insight about the relationship of the gas kinematics to the disk plane. If extended disks produced all the Mg II absorption, then we would expect the equivalent widths to correlate better with disk radius  $R$  than they do with impact parameter. We confirm that  $\langle W(b) \rangle$  decreases with increasing  $R$  ( $r_S = -0.47, 2.5\sigma$ ), as expected based on the well-established correlation between  $\langle W(b) \rangle$  and  $b$  ( $r_S = -0.56, 3.0\sigma$ ). Projection onto the disk plane does not increase the correlation coefficient, however, so the Mg II kinematics do not support a pure disk description, a result that was already clear from the velocity widths of Mg II systems. The open question is which absorp-

<sup>6</sup> Four of the 33 galaxy – quasar pairs with Mg II detections are excluded from this section. Following Ho et al. (2017), we exclude the J124601.81+173156.4 and J103640.74+565125.9 sightlines because the absorbers may not be related to the CGM of the target galaxy. Our NIRC2 imaging resolved J142815.41+585442.1 and J154956.73+070056.0 into multiple galaxies, so we could not measure their rotation curves and therefore exclude them as well.

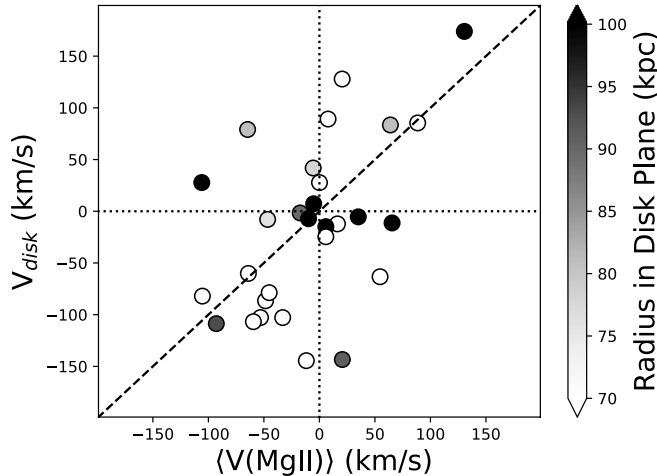


**Figure 14.** Disk model versus Mg II Doppler shifts. The gas in the model lies in the plane defined by the galactic disk and moves on circular orbits. This projected velocities of this model are positively correlated with the  $\langle V(MgII) \rangle$  measurements. The correlation is strongest among the sightlines that intersect the disk plane at radii  $R < 70$  kpc. The Spearman rank order correlation coefficient is  $r_S = 0.64$  for this subset of the data, which rules out the the null hypothesis (no correlation) at the  $2.4\sigma$  level.

tion components are consistent with absorption near the disk plane.

We again use the ratio of the Mg II equivalent width to  $\langle W(b) \rangle$ , the absorption excess, to take out the well-measured decline in absorption strength with impact parameter. Excess absorption appears as large symbols in Figure 15. The sightlines with the largest absorption excess intersect the disk plane at  $R > 80$  kpc, where the  $\langle V(MgII) \rangle$  velocities are not very correlated with the projected disk rotation. We therefore conclude that most the systems with excess absorption include velocity components *not* associated with gas in the disk plane. Outflowing gas far above the disk plane, for example, may contribute velocity components to these systems.

We find the largest absorption excess in the J091954+291408 sightline, which is near the major axis ( $\alpha = 15.3^\circ$ ). The J091954+291508 sightline is unique within our sample, as it shows two well separated Mg II components. We have interpreted the stronger component, which is redshifted with respect to the systemic velocity, as the one associated with the target galaxy. This stronger component corotates with the galactic disk, following the trend for low azimuthal angle sightlines. The symbol size in Figure 15 represents only this stronger component. This sightline impacts the disk plane at  $R = 115$  kpc. Previous work has shown that the CGM extends to larger radii around group galaxies (Bordoloi

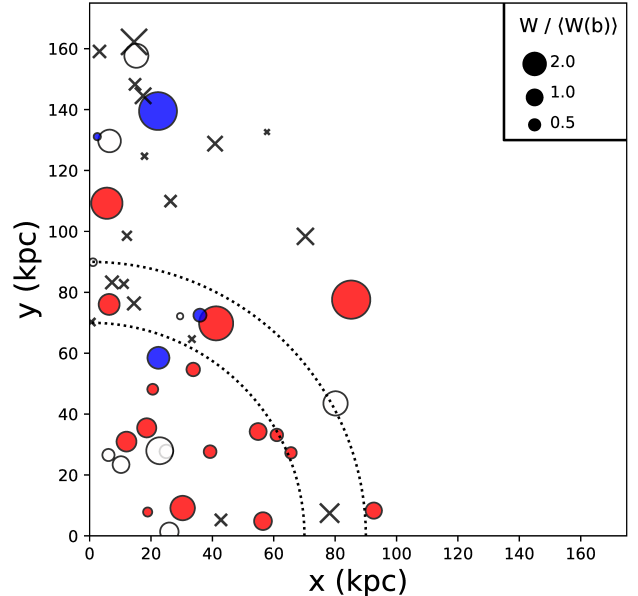


**Figure 15.** Relative Mg II absorption strength in the disk plane. Symbol color represents corotation (red), counter rotation (blue), and systemic velocity (white) with respect to circular orbits in the disk plane. We scale the symbol size by  $W_r / \langle W_r(b) \rangle$ , where the black line in Figure 6 defines the expected absorption strength  $\langle W_r(b) \rangle$  as measured by Nielsen et al. (2013). The lines show disk radii of  $R_{max} = 70$  and 90 kpc. The sightlines with the largest excess equivalent width intersect the disk plane at  $R \geq R_{max}$ . We conclude that absorption from an extended disk is unlikely to be the primary source of the excess absorption.

et al. 2011; Johnson et al. 2015; Nielsen et al. 2018), and the environment of J091954+291345 may contribute to the excess absorption.<sup>7</sup> The second component may be associated with a different galaxy or a group. Tidal streams generated by a galaxy – galaxy interaction may contribute to one or both of these absorption components.

Galactic outflows produce most of the equivalent width, however, in the three systems with the next highest absorption excesses. In the next section, we present a strategy for recognizing galactic outflows and

<sup>7</sup> We find evidence that our target galaxy J091954+291345 is involved in an interaction with other group members. The NIRC2 image shows a prominent 2-arm spiral that may be two tidal tails. The candidate group includes two luminous galaxies with red colors in addition to our target. Spectroscopic redshifts are needed to confirm these potential group members: (1) J091954+291345 is  $4''.4$  from our target and has a similar impact parameter, and (2) J091954+291336 is  $8''.7$  from our target and further than our target from the quasar sightline.

then show that these absorption-line profiles are inconsistent with a disk component but easily described by a simple outflow model. We return to the disk-like component in Section 4.3 where we use non-detections to further constrain their properties.

#### 4.2. Outflow Component

Galactic winds blow out of disks along the path of least resistance, forming bipolar structures whose axis is perpendicular to the disk plane (De Young & Heckman 1994). Cool, dense outflows within a few kpc of galaxies have been directly imaged in optical emission lines (Lehnert & Heckman 1995; Martin 1998). Mapping the Doppler shifts across these nebulae reveals multiple velocity components whose separation and relative strength are well described by the surface of a conical structure (Heckman et al. 1990). The term *galactic wind* was originally introduced to describe the much hotter fluid inside this cone (Chevalier & Clegg 1985); yet x-ray emission from hot winds has only been detected from a few nearby starburst galaxies (Strickland et al. 2000). The cooler component, which we will call the *outflow* to distinguish it from the hot wind, has been detected via blueshifted absorption lines in galaxy spectra across much of cosmic time (Heckman et al. 2000; Martin 2005; Martin et al. 2012; Erb et al. 2012; Kornei et al. 2012; Rubin et al. 2014). The broad absorption component from an outflow typically overlaps the absorption component from interstellar gas (Martin et al. 2012). This line blending complicates measurements of outflow properties. We chose quasar sightlines that avoid the interstellar medium, eliminating this confusion.

The schematic drawing in Figure 16 illustrates the intersection of a quasar sightline and an outflow. Outflow opening angles range from  $\theta_{max} = 30^\circ$  to  $45^\circ$  at intermediate redshift based on the fraction of galaxy spectra with outflow detections (Martin et al. 2012). Moving the quasar closer to the minor axis on the sky produces a wider parabola in the  $x = x_0$  plane, reaching the opening angle of the cone for a minor-axis sightline. Sightlines close to the minor axis therefore intercept outflowing gas over the largest pathlengths. Assuming clouds populate the outflow cone, the longer pathlengths increase the range of observed Doppler shifts. We attribute the observed increase in Mg II equivalent widths with increasing azimuthal angle to this geometrical effect.

A degeneracy regarding which side of the minor axis is tipped toward the observer presents a problem, allowing outflowing gas to be either redshifted or blueshifted in a quasar sightline. The Doppler shift of the Mg II system does not uniquely identify outflowing gas the way it identifies corotating gas. The left-hand panels of Fig-

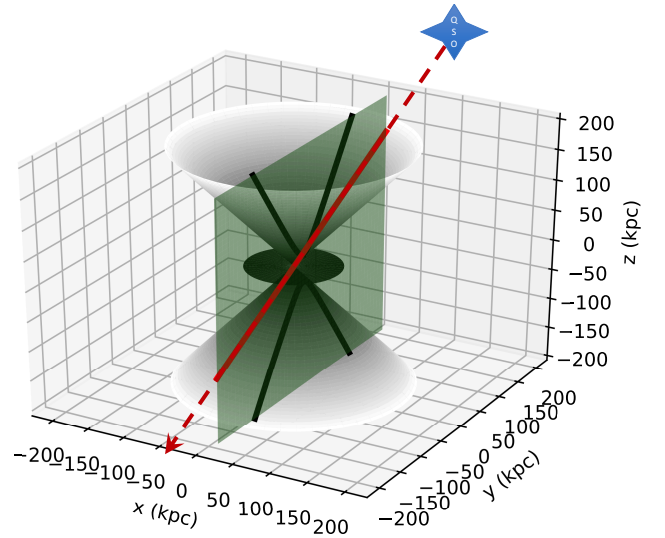


**Figure 16.** Coordinate system describing the three-dimensional geometry of a galactic disk and bipolar outflow. The outflow is radial in a cone perpendicular to the disk. Clouds of low-ionization gas could populate the interior of the cone or be concentrated along its surface. The angular momentum vector of the disk defines the direction of the z-axis. The angle between the z-axis and the cone defines the *outflow opening angle*,  $\theta_{max}$ . The positive x-axis corresponds to the receding side of the major axis. A quasar sightline lies in a plane at  $x = x_0$ . The intersection of this plane with the outflow cone defines a parabola. The observer lies at a negative  $y$ -coordinate approaching infinity.

ure 17 illustrate the projection of outflow cone on the sky.

Determining which side of the disk is tipped toward the observer eliminates the ambiguity. Figure 17 illustrates a strategy for measuring the *3D orientation* of the disk. In a self-gravitating, collisionless system, only trailing spiral patterns are long lived (Carlberg & Freedman 1985). Most spiral patterns therefore lag further behind the direction of rotation with increasing radius. A rotation curve and the winding direction of the arms determine the disk tilt, leading to a complete description of the disk orientation in three-dimensional space.

The F390W images resolve spiral patterns. The winding direction of the arms is apparent in roughly 20% of the *Ks* images. Figures 2, 3, and 4 show examples. We define the sign of the disk inclination as shown in Figure 17. Images and measurements for galaxies probed with major-axis sightlines are presented in Ho et al. (2019, in prep). Table 2 lists the signed inclinations for galaxies observed with sightlines at large azimuthal angles. We use the 3D orientations of these disks to

predict the velocity range of an outflow component and then discuss whether an outflow is detected below.

We will use the terms blueshifted-lobe and redshifted-lobe to describe the Doppler shift of gas moving radially outward along the symmetry axis of the cone. The lobe seen in front of the disk plane will have a net blueshift, while the lobe behind the disk plane will have a net redshift. The disk plane behind the blueshifted lobe is tipped away from the observer, while the near side of the disk plane will be seen in front of the redshifted lobe. This red/blue nomenclature identifies each outflow lobe but is a bit misleading. A single lobe may produce both redshifted and blueshifted absorption in a sightline. In Figure 17 for example, the near and far sides of the cone would acquire opposite Doppler shifts if the opening angle and/or inclination were increased. A quasar sightline may also intersect opposite lobes of a cone, but this geometry is not relevant in this paper because we selected disks viewed at high inclination.

We assume clouds populate the interior of the cone as well as its surface in order to illustrate the full range of velocity components that an outflow could produce. The outflow model has a constant radial velocity  $v_r$  which can be increased (decreased) to broaden (shrink) the predicted velocity range. We constrain the opening angle  $\theta_{max}$  independently. In principle the line profiles contain additional information related to the radial density gradient, which we do not model here because our spectra do not resolve the absorption components.

#### 4.2.1. Outflow Dominated Mg II Systems

We selected Mg II systems likely to be outflow dominated from the subsample for which we resolved spiral arms. These systems have excess equivalent width and are found in minor-axis sightlines. Our high-resolution images resolve spiral arms in seven galaxies meeting these criteria. Their equivalent widths range from 2 to 6 times the average at their impact parameters. Among them, our test is most sensitive for three that are orientated in ways that cleanly separate outflow and disk components. Their images are shown in Figure 18, and we discuss them in turn. We have applied unsharp masking techniques to some of the  $Ks$  images to enhance visibility of the arms (Ho et al. 2019, in prep).

The J095424+093648 sightline is near the minor axis of our target, J095423+093711. The projected rotation speed where the sightline intersects the disk plane is  $+28 \text{ km s}^{-1}$ , barely distinguishable from the systemic velocity. If the spiral arms seen in Figure 18 are trailing, then the inclination of the disk is positive, and our sightline would pass through the blueshifted lobe of an outflow before intersecting the disk plane at radius

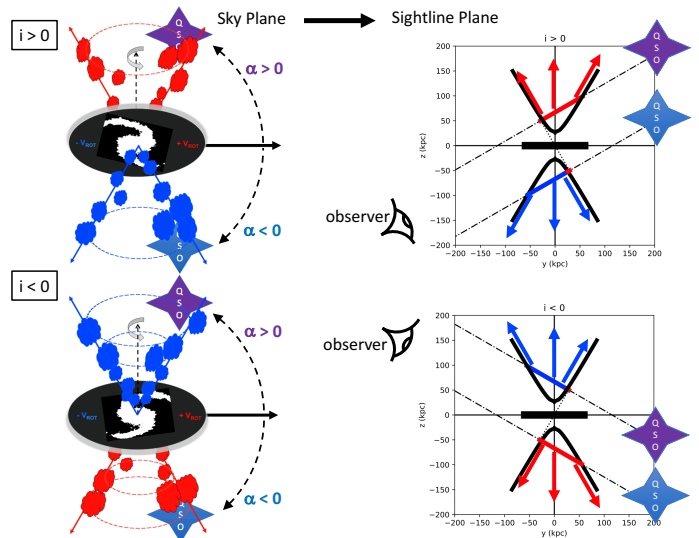


**Figure 17.** Geometry connects the sky plane to the sightline plane. *Left:* The image on the sky is rotated to align the rotation axis of the disk with the  $z$ -axis of the coordinate system; then the redshifted side of the rotation curve is on the right. The disk tilts shown in the top and bottom panels can be distinguished by the winding direction of the spiral arms. Determining the sign of the disk inclination this way makes a unique prediction for the sign of the Doppler shift from a conical outflow. *Right:* Schematic view of the outflow cone in the plane of the sightline. Positive and negative values of the azimuthal angle are shown. Along each sightline (dot-dash lines), the sign of the projected radial outflow velocity is denoted as redshifted (red) or blueshifted (blue).

$R = 141 \text{ kpc}$ . We detect a blueshifted Mg II system at  $\langle V(MgII) \rangle = -106 \text{ km s}^{-1}$ . A radial outflow speed of  $180 \text{ km s}^{-1}$  combined with an outflow opening angle of  $30^\circ$  describes the observed velocity range of Mg II absorption in Figure 19. No absorption is detected at the velocity of the disk component. The line profile shows a weaker, second component blueward of the strongest component. The sightline geometry, see the left panel of Figure 19, shows that the outflow absorption comes from increasingly larger radii as the blueshift increases, qualitatively explaining the line profile shape. Increasing the opening angle much beyond  $\theta_{max} = 30^\circ$  would generate a redshifted component from the outflow that is not observed in the Mg II line profile.

The disk of J145844+170522 has a positive inclination. Figure 18 shows that the J145844+170514 sightline intersects the near side of the disk plane at  $R = 63 \text{ kpc}$  before encountering the redshifted outflow lobe. The azimuthal angle,  $\alpha = 123.4^\circ$ , places the quasar  $33.4^\circ$  from the minor axis. In this geometry, the Doppler shift of an outflow component would distinguish it from

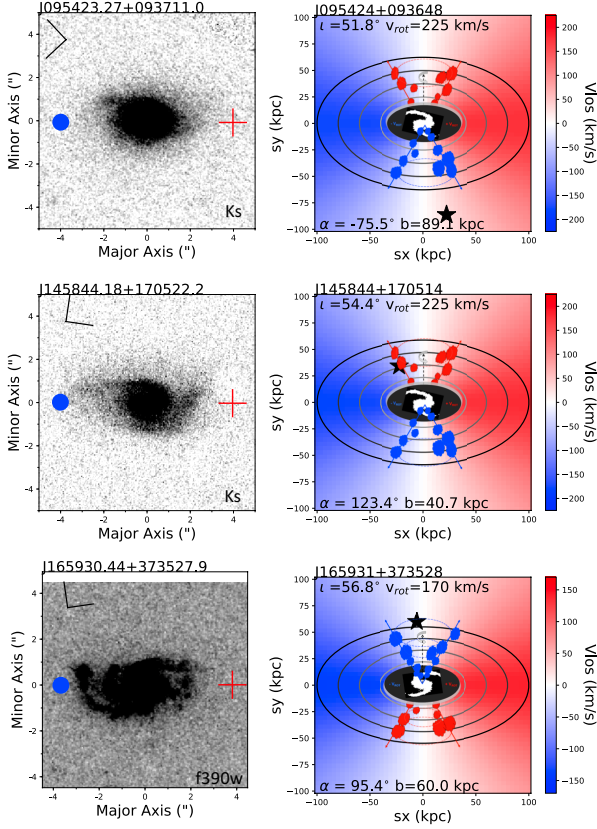


**Figure 18.** Examples of galaxies oriented in ways that produce outflow and disk plane components which can be easily distinguished. *Left:* Detection of spiral arms. For ease of comparison, we orient the galactic disks so that the receding side of the major axis (red plus) is on the right; the compass rose indicates north and east on the sky. If the spiral arms are trailing, then the disks are tipped as shown in the schematic to the right. *Right:* Schematic of outflow cone projected onto the velocity field in the plane of an extended disk. For a positive disk inclination, the bottom lobe of the outflow cone is the closer, blueshifted side. The black star marks the quasar sightline. In two of these examples, the net absorption from the outflow has the opposite sign of gas rotating in the disk plane. In the third example, a disk component has a projected speed close to the systemic velocity.

a disk component. The projected rotation speed is  $-63 \text{ km s}^{-1}$ . We measure a net redshift for the Mg II system, which is one of just a few counter-rotating systems at  $R < R_{max}$ . Figure 19 shows that the projected velocity range of a  $v_r = 100 \text{ km s}^{-1}$  outflow overlaps the strongest absorption component. A weaker disk component may produce the blended, blueshifted component, a prediction we hope to test with higher resolution spectroscopy. The outflow component clearly produces the equivalent width excess.

Our high resolution images draw attention to the disturbed morphology of J165930+373527; a large arm extends southward wrapping towards the east. The wrapping direction of the arms and the rotation curve require a negative disk inclination if the arms are trailing. In this orientation the quasar sightline intersects the blueshifted outflow lobe. The main absorption component is much more blueshifted than expected for a galactic disk component in this sightline. We infer an outflow speed of roughly  $100 \text{ km s}^{-1}$ , about  $20 \text{ km s}^{-1}$  higher than Kacprzak et al. (2014) fit because we measure a correspondingly higher galaxy redshift. Figure 19 shows that outflow angles approaching  $\theta_{max} \gtrsim 45^\circ$  produce some redshifted absorption; but the blue component limits the fitted outflow speed such that the outflow cone does not describe the prominent red wing on the Mg II line profile even if  $\theta_{max}$  approaches  $90^\circ$ . It is possible that the redshifted absorption wing is produced by streams associated with the interaction driving the tidal arm. The target galaxy is isolated in the sense that there are no brighter galaxies with a consistent (photometric) redshift within 100 kpc.

#### 4.2.2. Multi-component Sightlines

Figure 20 shows more minor-axis sightlines near resolved galactic disks. These systems also have stronger than average Mg II absorption. Their geometry is less favorable for distinguishing outflow and disk components, which have similar line-of-sight velocities, so we do not fit an outflow speed in these cases. We adopt an outflow speed of  $v_r = 150 \text{ km s}^{-1}$  and illustrate the velocity range where this outflow would contribute to the line profile in Figure 20.

The J122413+495515 disk has a positive inclination. The J122411+495511 sightline intersects the redshifted half of the disk plane at  $R = 81 \text{ kpc}$ . The azimuthal angle is not close enough to the minor axis to intersect a  $\theta_{max} \approx 30^\circ$  outflow cone. A large opening angle is required to produce an outflow component. The narrow absorption component produced by the fiducial  $150 \text{ km s}^{-1}$  outflow speed and opening angle  $\theta_{max} = 45^\circ$  is coincident with a disk component. Increasing the outflow speed to  $v_r \approx 200 \text{ km s}^{-1}$  will spread the outflow absorption across the redshifted line wing visible in the last column of Figure 20. A very large opening angle, roughly  $\theta_{max} > 52^\circ$ , would also produce the blueshifted component. The line profile appears to be a blend of multiple, unresolved components. A disk model can only explain a single, narrow component. An outflow with a large opening angle can explain the broad range of absorption velocities.

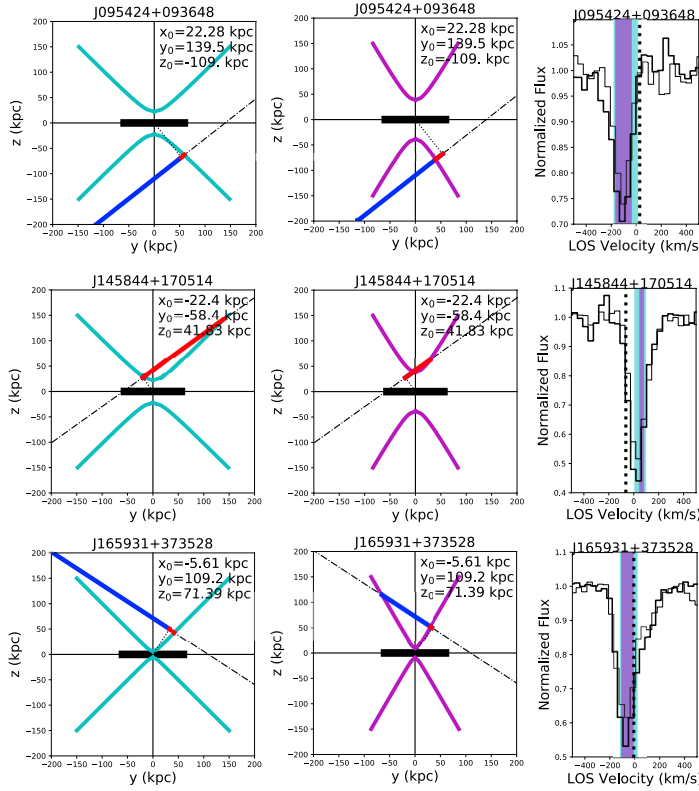


**Figure 19.** Intersection of outflow cones with the plane of the quasar sightline. For two values of the cone’s opening-angle, a radial outflow within the boundaries of each cone is projected onto the quasar sightline. The color along each sightline denotes the sign of the observed Doppler shift. The right most panels show the Mg II  $\lambda 2796$  (bold line) and  $\lambda 2803$  (thin line) line profiles relative to the target galaxy systemic velocity. We overlay the line-of-sight velocity range for outflow speeds  $v_r = 180, 100$ , and  $120 \text{ km s}^{-1}$  for J095424+093648, J145844+170514, and J165931+373528, respectively. The wider cone with  $\theta_{max} = 45^\circ$  predicts absorption velocities within the cyan band, and the purple band shows the velocity range across the  $\theta_{max} = 30^\circ$  cone.

The absorption near the galaxies J123249+433244 and J133541+285324 likely includes an outflow component for several reasons. The J123249+433244 and J133542+285330 sightlines are not only close to the minor axis; they also intersect the disk plane at very large radii. The Mg II systems are fairly weak in absolute terms, but their equivalent widths are twice the predicted value for their large impact parameter. Both sightlines intersect outflow cones with a wide range of opening angles. Outflowing gas would be blueshifted along most of each sightline. However we predict substantial absorption from these outflows near the systemic velocity. The radial velocity vector is nearly per-

pendicular to our sightline on the far side of the cone in Figure 20, which is where the radius is small and the outflow density highest.

The absorption system associated with J153546+291932 has a narrow, asymmetric component which is blueshifted and a weaker blueshifted line wing at  $-200 \text{ km s}^{-1}$ . Figure 20 shows that our sightline is nearly parallel to the surface of an outflow cone  $\theta_{max} \approx 45^\circ$ , generating both a long pathlength through the outflow and very little deprojection of the outflow velocity. This geometry may provide better than average sensitivity to the fastest, lowest column regions of the outflow. Fitting the broad blue wing requires low-ionization outflow moving at  $v_r \gtrsim 200 \text{ km s}^{-1}$ . At our fiducial outflow speed of  $150 \text{ km s}^{-1}$ , outflowing gas would contribute to the narrow, blueshifted component, which may be blended with an absorption component produced nearer the disk plane. The sightline intersects the disk plane at a relatively small radius  $R = 33 \text{ kpc}$ .

#### 4.2.3. Properties of Outflows & Their Host Galaxies

We have presented the most secure outflow detections. Six of these seven galaxies have SFRs slightly above the SFR main sequence in Figure 1, the exception being J123249+433244 with specific  $SFR = 0.068 \text{ Gyr}^{-1}$ . The highest estimated specific SFR is  $0.81 \text{ Gyr}^{-1}$  in J165930+373527. We identified four starburst galaxies in Section 2.4.2 with higher specific SFRs. The minor-axis sightline probing J133740+055211 intersects the disk plane where the line-of-sight velocity is just  $-8 \text{ km s}^{-1}$ , so this pair has a good geometry for distinguishing outflow and disk components. The equivalent width excess of  $W_r / \langle W(b) \rangle = 1.7$  also favors an outflow detection. The detected Mg II absorption is Doppler shifted  $-47 \text{ km s}^{-1}$ , which is consistent with an outflow if (and only if) the disk inclination is positive. High-resolution blue imaging with HST would resolve the spiral arms in the disk, allowing us to measure its 3D orientation and test this outflow prediction.<sup>8</sup>

We identified spiral arms and measured the disk inclinations for five other galaxies whose CGM was detected in a sightline near the minor axis ( $\alpha > 45^\circ$ ). Three of the associated sightlines address the question of whether weaker than average Mg II systems also detect outflows. The strongest case for an outflow among

<sup>8</sup> Our sightlines do not constrain the outflow properties of the other three starburst galaxies. The NIRC2 imaging resolves spiral arms in only one of the starburst galaxies, J123049+071050, which is paired with a major axis sightline ( $\alpha = 4.0^\circ$ ) that does not intersect a conical outflow. The sightline paired with J150150+553227 does not detect Mg II, and the NIRC2 image resolved J142815+585442 into two galaxies.

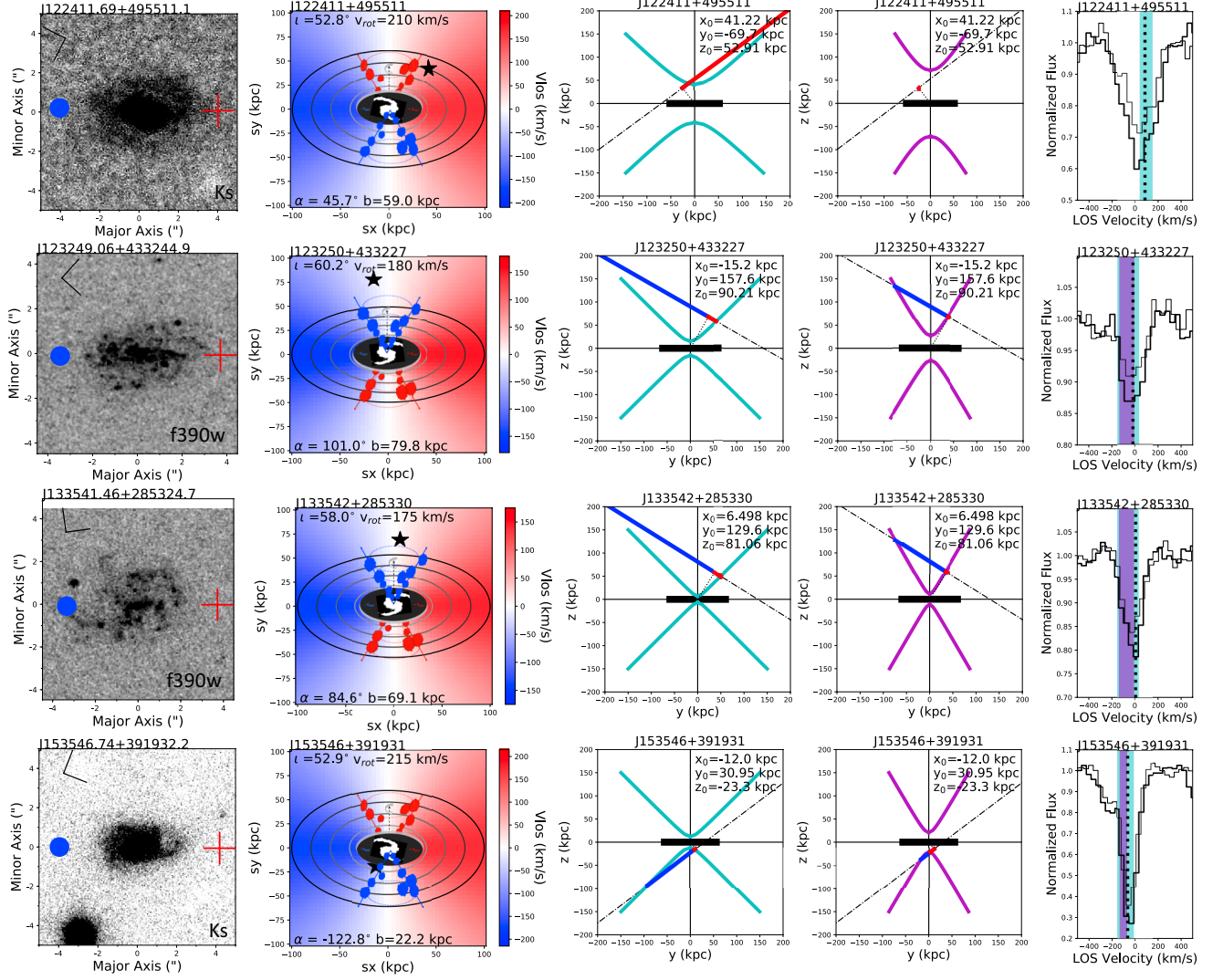


**Figure 20.** Examples of Mg II absorption systems with blended velocity components *and* a measured 3D disk orientation that constrain the geometry. We compare the line profile to the projected velocity of rotation in the disk plane (vertical, dotted line) and outflow cones with opening angles of  $45^\circ$  (cyan band) and  $30^\circ$  (purple band). With no tweaking of any parameter, a fiducial outflow speed  $v_r = 150 \text{ km s}^{-1}$  provides an explanation for the redshifted component in the J122411+495511 sightline and the blue wing in the J153546+391931 sightline.

these is in the J155504+362847 spectrum which detects absorption 34 kpc from J155505+382848 at 0.46 of the average equivalent width. The  $K_s$  image marginally resolves a tightly wrapped two-arm spiral pattern that would require a negative disk inclination, but the wrapping direction is not as certain as it is for the other spiral patterns discussed in this paper. Higher signal-to-noise ratio blue imaging needs to be obtained; but if the preliminary 3D orientation is correct, an outflow cone will produce blueshifted absorption in the quasar sightline between roughly  $-145$  and  $-14 \text{ km s}^{-1}$ . This sightline intersects the disk plane at  $R = 52 \text{ kpc}$  where circular orbits project to a line-of-sight velocity of  $-78 \text{ km s}^{-1}$ . We measure a Mg II Doppler shift of  $-45 \text{ km s}^{-1}$ , con-

sistent with either disk plane or outflow absorption. It seems likely that both components are detected because the line profile shows two blended, blueshifted components.

We measure positive inclinations for the disks of J143603+375138 and J154956+070056. The Mg II equivalent widths in the J143603+375131 and J154956+070056 sightlines are, respectively, 0.20 and 0.32 times the average value for the impact parameters. Our analysis for these pairs does not rule out outflows, but it does not offer compelling evidence for outflows either. For example, the J143603+375131 sightline selects the blueshifted outflow lobe but also intersects redshifted outflowing gas on the far side of this lobe.

The Mg II absorption is near the systemic velocity,  $\langle V(MgII) \rangle = +35_{-10}^{+4}$  km s<sup>-1</sup>. Similarly, a 150 km s<sup>-1</sup> outflow from J154956+070056 would produce absorption at Doppler shifts from -142 km s<sup>-1</sup> to +46 km s<sup>-1</sup> relative to the target galaxy systemic velocity in the J154956+070056 spectrum. This sightline intersects the disk plane at  $R = 48$  kpc where the projected rotation speed is positive but near the systemic velocity. We detect Mg II absorption at the systemic velocity.

Our analysis rules out outflow detections in some sightlines. We have already seen in Figure 7 that some minor-axis sightlines do not detect a Mg II system. In addition, we resolve spiral patterns in the NIRC2 imaging that require a positive disk inclination for J135051+250506 and a negative disk inclination for J152027+421519. The blueshifted Mg II system in the J1520228 sightline is not consistent with the projected outflow speeds of 25 to 245 km s<sup>-1</sup> (for  $\theta_{max} = 45^\circ$  and  $v_r = 150$  km s<sup>-1</sup>). The J135051+250506 sightline only intercepts outflows with a large opening angle,  $\theta_{max} \gtrsim 45^\circ$ , and the implied Doppler shifts are redshifted 78 - 148 km s<sup>-1</sup>, which is inconsistent with the Mg II system detected at the systemic velocity. Whether these non-detections indicate the absence of outflows from the target galaxies is not immediately clear. Alternatively, the covering fraction of low-ionization gas entrained in the winds may be less than unity.

The Mg I detections include some of these outflow systems. The velocity of the main Mg I absorption in the J165931+373528 spectrum corresponds to the main Mg II component, which we have attributed to absorption from a galactic outflow. The Mg I absorption velocity is coincident with the outflow component in J145844+170514. Our weakest Mg I detection is in the J122411+495511 spectrum, and the low SNR does not constrain the Mg I velocity very well. We explained in Section 2.5 why Mg I detections may indicate the presence of dense gas. Detection of Mg I absorption in two of our three strongest outflow systems may indicate the presence of dense clumps of gas in the outflows.

We found both outflow systems and corotating systems associated with galaxies having estimated halo masses exceeding  $10^{12} M_\odot$ . Galaxy formation theory has increasingly emphasized the importance of a critical halo mass of roughly  $10^{12} M_\odot$  (Kereš et al. 2005; Dekel & Birnboim 2006), above which gas accretion fed by cold flows is greatly suppressed. In Table 2 we list 11 galaxies with halo masses in the range  $12.01 < \log M_h < 12.63$ . However abundance matching introduces factors of two-ish (at the one-sigma level) uncertainties when applied to an individual galaxy (Behroozi et al. 2010). Even our targets with the highest stellar masses have

blue colors. This selection may bias them toward the lower end of the halo mass range for their stellar mass, perhaps explaining why their CGM absorption properties do not stand out. The more significant statement is that the median halo mass of our sample is a factor of 2.5 lower than the theoretical critical mass, offering an explanation for why cold flow disks would still be forming at low redshift.

#### 4.3. The Maximum Extent of Corotating Gas

Our Quasars Probing Galaxies program does not find an edge, or maximum extent, for the corotating CGM. The results of Section 4.1 require the corotating structure be non-axisymmetric at radii  $R \gtrsim R_{max} \approx 70 - 80$  kpc. Gas streams are one such example. Streams produced by cold flow gas (Stewart et al. 2011a,b) or satellite winds (Anglés-Alcázar et al. 2017; Hafen et al. 2018) have both been shown to feed the growth of extended disks in numerical simulations. These streams have smaller covering fractions than do the warped disks (Stewart et al. 2013) and offer a plausible explanation for the corotation we observe at  $R > 70$  kpc.

This result motivates an examination of corotation at larger impact parameters. Our sightlines probe the inner CGM. Observations of absorption-line-systems already exist at larger impact parameters, but the rotation curves and orientations of the host galaxies have not typically been measured. One complication will be that the strength of low-ionization metal lines decreases rapidly toward larger impact parameters.

It has recently been argued that low-ionization absorbers lie at much smaller radii than the high-ionization gas producing O VI absorption (Stern et al. 2018). Combining the COS-Halos and Johnson et al. (2015, 2017) measurements, the equivalent width - impact parameter relation for O VI is less steep than that for the lower ionization metal lines (Stern et al. 2018). Heckman et al. (2017), however, showed the strength of the metal lines falls off more slowly (like the O VI) in the CGM of starburst galaxies. It is not clear whether detections of low-ionization lines at  $b \geq 0.5r_v$  require a starburst. Indeed, the duration of starburst activity (by definition almost) is limited to the dynamical timescale of the galaxy, which is short compared to that of the halo on spatial scales 10 to 100 times larger.

High ionization lines including Ne VIII (Burchett et al. 2018) as well as O VI will probably be the tool of choice to investigate CGM kinematics on larger scales. While neutral hydrogen is also detected at large impact parameters, the metal lines are more biased towards gas clouds that lie within the virial radius. Hydrogen gas beyond the virial radius can produce absorption near the sys-

temic velocity because of well-known degeneracies between Doppler shifts induced by peculiar velocities and cosmological redshift.

Comparing the angular momenta of the gas traced by O VI and Mg II systems could yield new insight the origin of O VI systems. We note that inner CGM sightlines with O VI detections often show some kinematic correspondence with the low-ionization components (Werk et al. 2014). The high ionization systems are often offset to one side of the systemic velocity, so some O VI components may corotate with the galaxy. High-ionization gas behind virial shocks has recently been shown to have significant rotation in cosmological hydrodynamical simulations (Oppenheimer 2018). In an alternative picture, where the O VI lies at much larger radii (Stern et al. 2018), the high-ionization gas feeds a reservoir of low-ionization gas as it cools, so the O VI absorption would be Doppler shifted with the same sign as the Mg II systems but have smaller absolute velocity shifts than the low ions.

We searched the HST archives and found COS observations for two of our targets. The J155504+362847 sightline has an intermediate azimuthal angle ( $\alpha = 44.6$ ); it intersects the disk at  $R = 55$  kpc. Figure 21 compares the projected line profiles to the projected rotation speed in the disk plane. The strongest component in the low-ionization lines is consistent with rotation in the disk plane, and this component is also the strongest O VI component. Corotating gas is detected in this O VI system. Several of the O VI absorption components, however, are more blueshifted than a disk component. Our ability to determine the velocity offset of an outflow component is limited by the marginal constraints on the sign of the disk inclination. The contrast of the spiral arms in our infrared image is poor, but our image processing suggests a negative disk inclination. An outflow component in the quasar sightline would then be blueshifted for this disk orientation, so the system may include one of more components from an outflow and/or a disk component.

The outflow dominated Mg II system, J165931+373528, is only marginally detected in O VI. The sightline is near the minor axis ( $\alpha = 84.6$ ). Apparently not all outflows produce strong O VI absorption. We do not draw any general conclusions from these two sightlines.

However Kacprzak et al. (2018) recently presented measurements of galactic rotation for the hosts of O VI absorption-line systems. They found no significant excess of corotating O VI. Clearly corotating O VI absorption is not ubiquitous. More comparisons of galaxy rotation curves to the gas kinematics in higher ioniza-

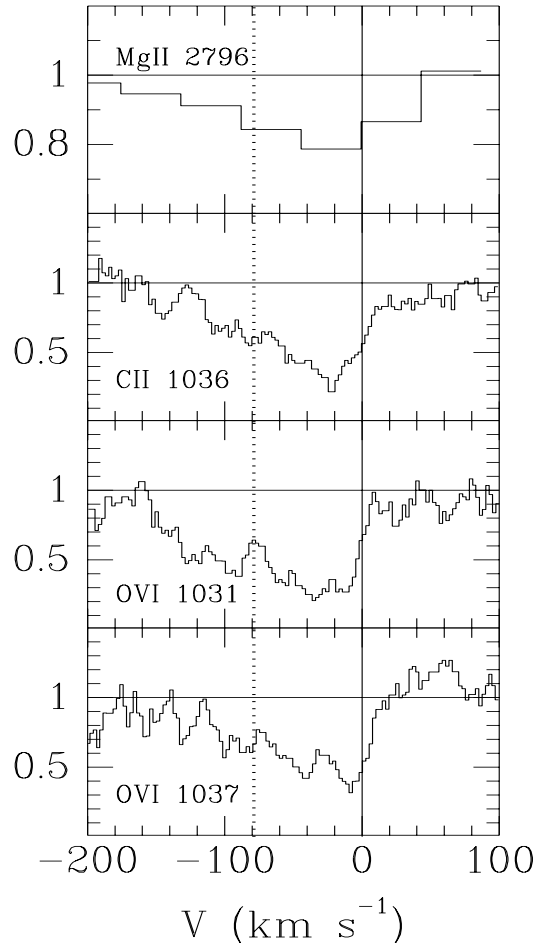


**Figure 21.** Absorption by the CGM of J155505.27+362848.4 in the spectrum of J155504.39+362847.9. The blue wing on the Mg II profile indicates multiple components, and these are better resolved by the C II detection in the HST/COS spectrum (GO 11598, PI Tumlinson). Absorption from O VI is detected over the same velocity range as the low-ion absorption. The asymptotic rotation speed of the galaxy,  $255 \text{ km s}^{-1}$ , projects to  $-105 \text{ km s}^{-1}$  along the quasar sightline ( $\alpha = 44.6^\circ$ ,  $i = 55.2^\circ$ ). Both the high-ionization and low-ionization CGM corotate with this galactic disk.

tion lines would clearly provide additional insight into the nature of corotating circumgalactic gas.

## 5. CONCLUSIONS

Circumgalactic gas flows that feed the disk fuel for star formation and those driven by feedback can be identified via the Doppler shifts and linewidths of metal-line absorption systems detected in spectra of background beacons. In this paper we investigated how the orien-

tation of galactic disks can be used to distinguish these components from other sources of low-ionization halo gas. We used LGSAO at Keck Observatory and HST to establish the orientation of the galactic disks on the sky. When the winding direction of spiral arms is measured, our rotation curve measurements determine the 3D orientation of the disk because long-lived spiral patterns trail the rotation direction.

Circumgalactic gas kinematics were measured relative to these disks. We observed 50 quasars located behind galaxies drawn at random from a well-defined population: star-forming galaxies with  $M_* \approx 10^{10} M_\odot$  at redshift  $z \approx 0.2$ . The Keck/LRIS spectra provide sensitivity to an absorber of average strength over the full range of impact parameters,  $b \approx 12 - 98$  kpc. We found the following results.

1. The equivalent-width weighted Doppler shifts of Mg II absorbers often show a net Doppler shift with the same sign as the galactic rotation. This comparison was made as a function of azimuthal angle at impact parameters  $b < 0.5r_{vir}$ . We found no examples of net counter-rotating absorption within  $45^\circ$  of the major axis. Corotation describes the velocity offsets of Mg II absorption over a larger range of azimuthal angles than we reported in Ho et al. (2017). Differences between the azimuthal distribution of corotators and counter-rotators depend on galaxy inclination, and our galaxy selection criteria favored edge-on disk orientations
2. Absorber strengths at fixed impact parameter generally increase with azimuthal angle. We found the opposite trend, however, at very small impact parameters; sightlines at  $b < 40$  kpc detect stronger Mg II systems near the major axis. The strong absorption requires multiple velocity components rather than exceptional column densities, so these trends identify kinematically disturbed circumgalactic gas.
3. We computed the Doppler shift for a velocity component generated by gas orbiting in the disk plane. When we could determine the sign of the disk inclination, we also predicted the line-of-sight velocities for an outflow component. Outflows uniquely fitted the observed Mg II velocity range for the minor-axis sightlines with the largest absorption excess, demonstrating that outflow components increase equivalent width near the minor axis at redshifts as low as  $z \approx 0.2$ . We found that the measured  $\langle V(MgII) \rangle$  values were positively correlated

with the projected disk velocities ( $r_S = 0.64, 2.4\sigma$ ) for the subset of sightlines that intersect the disk plane at  $R \leq 70$  kpc. This correlation draws attention to the important role of angular momentum in supporting the low-ionization CGM. Blending of multiple components in our spectra may weaken the significance of this correlation, something we plan to test with higher resolution spectroscopy.

Motivated by the result that a significant portion of the inner CGM is rotating in a manner related to the galactic disk, we make the following observations. Among all the sightlines that intersected the disk plane at  $R < 70$  kpc, only one failed to detect Mg II absorption, and only one detected counter-rotating absorption. We conclude that on scales  $R < 70$  kpc, the corotating CGM is likely axisymmetric, reminiscent of warped extended disks (Stewart et al. 2011a,b) but also consistent with corotating structures that are less flattened (El-Badry et al. 2018).

We emphasize that centrifugally supported disks fail to produce the full range of absorption velocities (Steidel et al. 2002; Kacprzak et al. 2010). One possible resolution is that the corotating gas is only partially supported by centrifugal forces, and it gradually spirals into the galactic disk, thereby broadening the line profile (Ho et al. 2017). Ho et al. (2019) measured inflow rates from a sample of simulated EAGLE galaxies with masses and redshifts matched to the work presented in this paper, and they found inflow rates in the disk plane sufficient to maintain current SFRs. It is therefore plausible that the corotating gas identifies material that feeds the growth of galactic disks at low redshift.

We did not detect a maximum impact parameter for corotation among  $\alpha < 45^\circ$  sightlines. The covering fraction of Mg II detections dropped, however, and their velocity offsets were no longer correlated with the galactic rotation speeds beyond  $R \gtrsim 70$  kpc. Inspection of numerical simulation paints a scenario in which streams feeding the disk produce corotation at these distances. Such streams extend well beyond the inner CGM in some simulations, so it will be important to directly measure velocity offsets at larger impact parameters than we considered in this work.

Radial outflow at  $120-180 \text{ km s}^{-1}$  within a cone easily described the velocity components producing the minor-axis excess equivalent width. This result would appear to conflict with numerical results indicating that individual clouds are destroyed on timescales much shorter than the time it would take to accelerate the cold gas (Scannapieco & Brüggén 2015; Brüggén & Scannapieco 2016; Schneider & Robertson 2017). Yet recent numer-

ical work has followed up on the cloud shattering argument of [McCourt et al. \(2016\)](#) and identified regimes where the cold gas not only survives but entrains many times its original mass through mixing layers with the hot wind ([Gronke & Oh 2018](#)). Hence it seems plausible that the interaction of a hot wind with the CGM triggers cooling that creates a low-ionization outflow, a scenario supported by high-resolution simulations of galactic winds ([Schneider et al. 2018](#); [Sparre et al. 2019](#)). We therefore wondered whether the low-ionization clouds might form beyond the galaxies at radii closer to the large impact parameters where we observe them.

We calculated the minimum radius where each of the seven sightlines intersects the surface of the outflow cone, finding values from  $r = 22$  kpc (J153546+391931) to 89 kpc (J095424+093648). A hot wind moving radially outward at  $v_r \geq 1000$  km s<sup>-1</sup> would disturb the ambient CGM at these radii on timescale of 22 to 87 Myr, short enough that the UV continuum would still be enhanced from the starburst. The Doppler shifts of the cooler outflows measured down-the-barrel in galaxy spectra are much slower ([Martin et al. 2012](#)). Taking  $v_r \approx 100$  km s<sup>-1</sup> for illustration, the timescale required to reach our sightlines grows to 220 to 870 Myr, and we might not identify the stellar population as a starburst. We therefore expect a stronger correlation between the outflow systems and the galactic SFRs in the scenario where a hot wind triggers the formation of the cold, low-ionization outflow that we detect in Mg II absorption.

Our sightlines through the halos of the four starburst galaxies happened to not be optimal for detecting outflows. Other work, however, has shown that equivalent widths are generally large in sightlines intersecting the CGM of starburst galaxies ([Heckman et al. 2017](#)) We have confirmed outflow components in seven galaxies with large absorption excesses, but they all have fairly normal star formation activity. The specific SFRs of the associated host galaxies range from 0.07 to 0.81 Gyr<sup>-1</sup>. It is possible that the detected outflows are relics of past starburst activity. Alternatively the feedback may be stronger than expected owing to additional acceleration mechanisms such as cosmic rays ([Everett et al. 2008](#); [Ruszkowski et al. 2017](#); [Jacob et al. 2018](#)).

The authors thank Sara Ellison, Andrey Kravtsov, and Jonathan Stern for useful discussions about this work. Some of the data presented herein were obtained at the W. M. Keck Observatory, which is operated as a scientific partnership among the California Institute of Technology, the University of California and the National Aeronautics and Space Administration. The Observatory was made possible by the

generous financial support of the W. M. Keck Foundation. The authors wish to recognize and acknowledge the very significant cultural role and reverence that the summit of Maunakea has always had within the indigenous Hawaiian community. We are most fortunate to have the opportunity to conduct observations from this mountain. The analysis presented in this paper was supported by the National Science Foundation under AST-1817125 (CLM). We gratefully acknowledge support for CWC from NSF AST-1517816. NASA supported the HST imaging analysis through grant HST-GO-14754.001-A from the Space Telescope Science Institute. GGK acknowledges the support of the Australian Research Council through the Discovery Project DP170103470. The two ESI rotation curve observations were obtained by Swinburne Keck program 2016A\_W056E. A portion of this work was performed at the Aspen Center for Physics, which is supported by National Science Foundation grant PHY-1607611

*Facility:* Keck:I (LRIS)

*Facility:* Keck:II (NIRC2)

*Facility:* Keck:II (LGSAO)

*Facility:* APO: (DIS)

*Facility:* HST: (COS)

*Facility:* HST: (WFC3)

**Figure Sets for Online Journal**

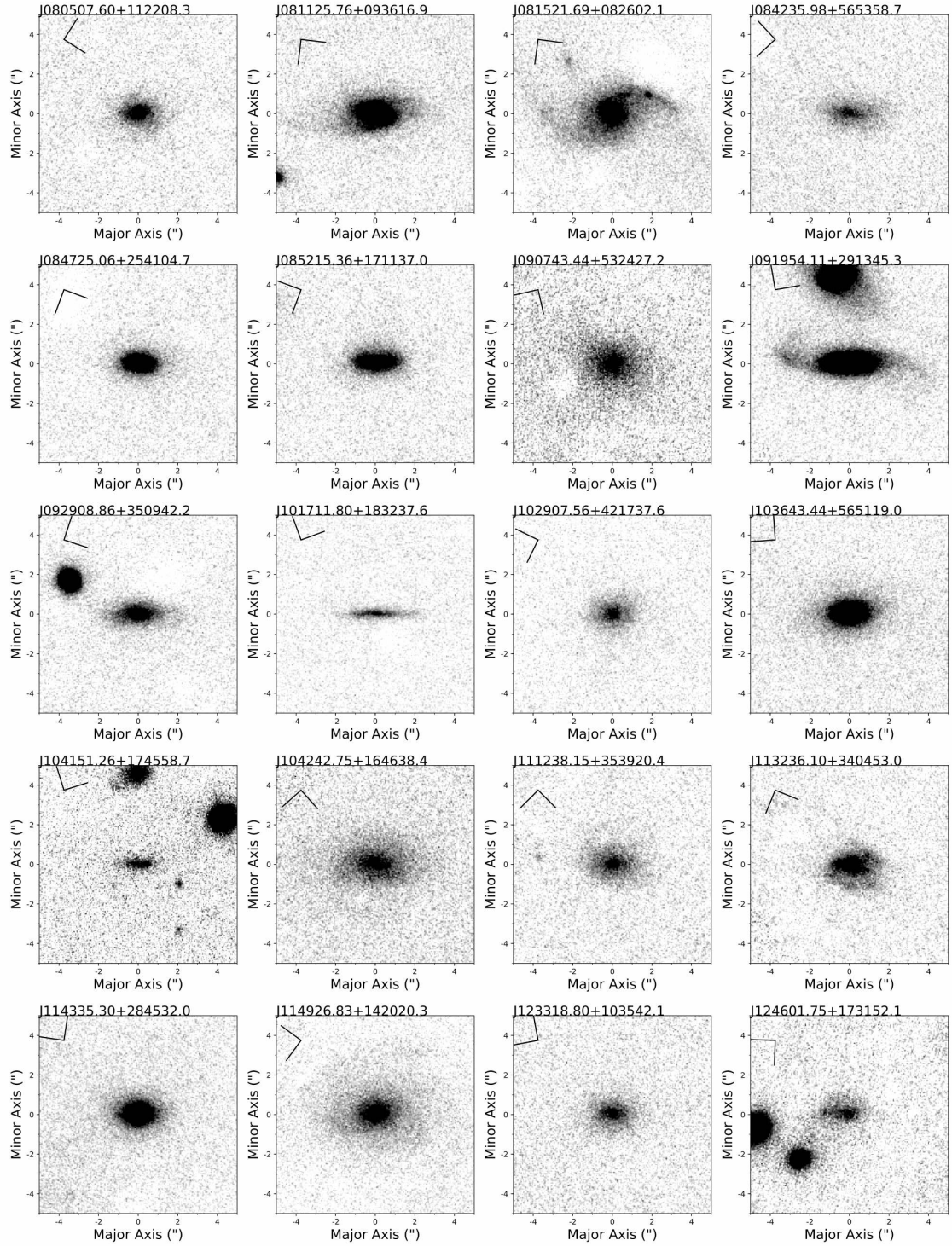


**Figure 3.** NIRC2/LGSAO  $K_s$ -band images. (b) - The NIRC2  $K_s$  band images of target galaxies that were not shown in the main text.

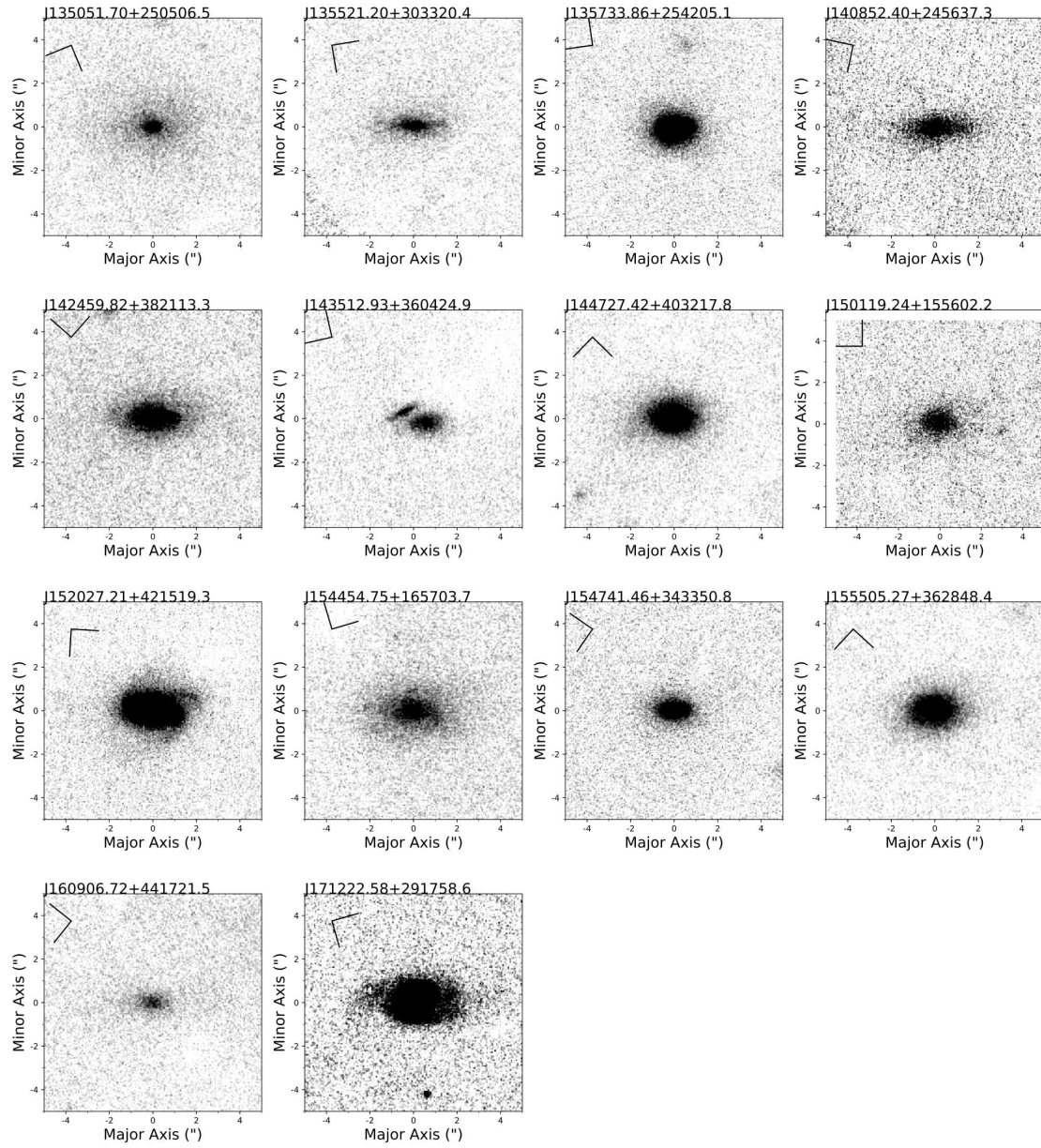


**Figure 3.** NIRC2/LGSAO  $K_s$ -band images. *c* - Continued from Figure 3b. Note that we did not obtain images of J142910+324840 and J150150+553227.

## REFERENCES

- Ahn, C. P., Alexandroff, R., Allende Prieto, C., et al. 2012, *ApJS*, 203, 21
- Anglés-Alcázar, D., Faucher-Giguère, C.-A., Kereš, D., et al. 2017, *MNRAS*, 470, 4698
- Barden, M., Rix, H.-W., Somerville, R. S., et al. 2005, *ApJ*, 635, 959
- Behroozi, P. S., Conroy, C., & Wechsler, R. H. 2010, *ApJ*, 717, 379
- Berg, T. A. M., Ellison, S. L., Tumlinson, J., et al. 2018, *MNRAS*, 478, 3890
- Bland-Hawthorn, J., Maloney, P. R., Stephens, A., Zovaro, A., & Popping, A. 2017, *ApJ*, 849, 51
- Blanton, M. R., Hogg, D. W., Bahcall, N. A., et al. 2003, *ApJ*, 594, 186
- Bordoloi, R., Lilly, S. J., Knobel, C., et al. 2011, *ApJ*, 743, 10
- Bouché, N., Hohensee, W., Vargas, R., et al. 2012, *MNRAS*, 426, 801
- Bouché, N., Murphy, M. T., Kacprzak, G. G., et al. 2013, *Science*, 341, 50
- Bouché, N., Finley, H., Schroetter, I., et al. 2016, *ApJ*, 820, 121
- Bowen, D. V., Chelouche, D., Jenkins, E. B., et al. 2016, *ApJ*, 826, 50
- Bregman, J. N., Anderson, M. E., Miller, M. J., et al. 2018, *ApJ*, 862, 3
- Brüggen, M., & Scannapieco, E. 2016, *ApJ*, 822, 31
- Bryan, G. L., & Norman, M. L. 1998, *ApJ*, 495, 80
- Burchett, J. N., Tripp, T. M., Prochaska, J. X., et al. 2018, *arXiv e-prints*, arXiv:1810.06560
- Carlberg, R. G., & Freedman, W. L. 1985, *ApJ*, 298, 486
- Chen, H.-W., Helsby, J. E., Gauthier, J.-R., et al. 2010, *ApJ*, 714, 1521
- Chen, H.-W., Prochaska, J. X., Weiner, B. J., Mulchaey, J. S., & Williger, G. M. 2005, *ApJL*, 629, L25
- Chevalier, R. A., & Clegg, A. W. 1985, *Nature*, 317, 44
- Churchill, C. W., Nielsen, N. M., Kacprzak, G. G., & Trujillo-Gomez, S. 2013a, *ApJL*, 763, L42
- Churchill, C. W., Trujillo-Gomez, S., Nielsen, N. M., & Kacprzak, G. G. 2013b, *ApJ*, 779, 87
- Danovich, M., Dekel, A., Hahn, O., Ceverino, D., & Primack, J. 2015, *MNRAS*, 449, 2087
- De Young, D. S., & Heckman, T. M. 1994, *ApJ*, 431, 598
- Dekel, A., & Birnboim, Y. 2006, *MNRAS*, 368, 2
- Diamond-Stanic, A. M., Coil, A. L., Moustakas, J., et al. 2016, *ApJ*, 824, 24
- El-Badry, K., Bradford, J., Quataert, E., et al. 2018, *MNRAS*, 477, 1536
- Ellison, S. L., Mallén-Ornelas, G., & Sawicki, M. 2003, *ApJ*, 589, 709
- Erb, D. K., Quider, A. M., Henry, A. L., & Martin, C. L. 2012, *ApJ*, 759, 26
- Everett, J. E., Zweibel, E. G., Benjamin, R. A., et al. 2008, *ApJ*, 674, 258
- Fall, S. M., & Romanowsky, A. J. 2018, *ApJ*, 868, 133
- Gauthier, J.-R., & Chen, H.-W. 2012, *MNRAS*, 424, 1952
- Ghez, A. M., Salim, S., Weinberg, N. N., et al. 2008, *ApJ*, 689, 1044
- Gogarten, S. M., Dalcanton, J. J., Williams, B. F., et al. 2010, *ApJ*, 712, 858
- González Delgado, R. M., Cid Fernandes, R., Garc´IRASa-Benito, R., et al. 2014, *ApJL*, 791, L16
- Governato, F., Willman, B., Mayer, L., et al. 2007, *MNRAS*, 374, 1479
- Governato, F., Brook, C., Mayer, L., et al. 2010, *Nature*, 463, 203
- Green, J. C., Froning, C. S., Osterman, S., et al. 2012, *ApJ*, 744, 60
- Gronke, M., & Oh, S. P. 2018, *MNRAS*, 480, L111
- Hafen, Z., Faucher-Giguere, C.-A., Angles-Alcazar, D., et al. 2018, *arXiv e-prints*, arXiv:1811.11753
- Heckman, T., Borthakur, S., Wild, V., Schiminovich, D., & Bordoloi, R. 2017, *ApJ*, 846, 151
- Heckman, T. M., Armus, L., & Miley, G. K. 1990, *ApJS*, 74, 833
- Heckman, T. M., Lehnert, M. D., Strickland, D. K., & Armus, L. 2000, *ApJS*, 129, 493
- Ho, S. H., Martin, C. L., Kacprzak, G. G., & Churchill, C. W. 2017, *ApJ*, 835, 267
- Hummels, C. B., Bryan, G. L., Smith, B. D., & Turk, M. J. 2013, *MNRAS*, 430, 1548
- Jacob, S., Pakmor, R., Simpson, C. M., Springel, V., & Pfrommer, C. 2018, *MNRAS*, 475, 570
- Johnson, S. D., Chen, H.-W., & Mulchaey, J. S. 2015, *MNRAS*, 449, 3263
- Johnson, S. D., Chen, H.-W., Mulchaey, J. S., Schaye, J., & Straka, L. A. 2017, *ApJL*, 850, L10
- Kacprzak, G. G., Churchill, C. W., Barton, E. J., & Cooke, J. 2011, *ApJ*, 733, 105
- Kacprzak, G. G., Churchill, C. W., Ceverino, D., et al. 2010, *ApJ*, 711, 533
- Kacprzak, G. G., Churchill, C. W., & Nielsen, N. M. 2012, *ApJL*, 760, L7
- Kacprzak, G. G., Martin, C. L., Bouché, N., et al. 2014, *ApJL*, 792, L12
- Kacprzak, G. G., Vander Vliet, J. R., Nielsen, N. M., et al. 2018, *ArXiv e-prints*, arXiv:1811.06028

- Kauffmann, G., Heckman, T. M., White, S. D. M., et al. 2003, *MNRAS*, 341, 33
- Kennicutt, Jr., R. C. 1983, *ApJ*, 272, 54
- Kereš, D., Katz, N., Weinberg, D. H., & Davé, R. 2005, *MNRAS*, 363, 2
- Kornei, K. A., Shapley, A. E., Martin, C. L., et al. 2012, *ApJ*, 758, 135
- Kriek, M., van Dokkum, P. G., Labbé, I., et al. 2009, *ApJ*, 700, 221
- Lan, T.-W., Ménard, B., & Zhu, G. 2014, *ApJ*, 795, 31
- Lan, T.-W., & Mo, H. 2018, *ApJ*, 866, 36
- Lehnert, M. D., & Heckman, T. M. 1995, *ApJS*, 97, 89
- Lochhaas, C., Thompson, T. A., Quataert, E., & Weinberg, D. H. 2018, *MNRAS*, 481, 1873
- Martin, C. L. 1998, *ApJ*, 506, 222
- Martin, C. L. 2005, *ApJ*, 621, 227
- Martin, C. L., & Bouché, N. 2009, *ApJ*, 703, 1394
- Martin, C. L., Dijkstra, M., Henry, A., et al. 2015, *ApJ*, 803, 6
- Martin, C. L., Shapley, A. E., Coil, A. L., et al. 2012, *ApJ*, 760, 127
- McCourt, M., Oh, S. P., O’Leary, R. M., & Madigan, A.-M. 2016, *ArXiv e-prints*, arXiv:1610.01164
- McCourt, M., O’Leary, R. M., Madigan, A.-M., & Quataert, E. 2015, *MNRAS*, 449, 2
- Morton, D. C. 2003, *ApJS*, 149, 205
- Moustakas, J., Coil, A. L., Aird, J., et al. 2013, *ApJ*, 767, 50
- Muñoz-Mateos, J. C., Boissier, S., Gil de Paz, A., et al. 2011, *ApJ*, 731, 10
- Nelson, D., Pillepich, A., Springel, V., et al. 2018, *MNRAS*, 475, 624
- Nielsen, N. M., Churchill, C. W., & Kacprzak, G. G. 2013, *ApJ*, 776, 115
- Nielsen, N. M., Kacprzak, G. G., Pointon, S. K., Churchill, C. W., & Murphy, M. T. 2018, *ApJ*, 869, 153
- Oke, J. B., Cohen, J. G., Carr, M., et al. 1995, *PASP*, 107, 375
- Oppenheimer, B. D. 2018, *MNRAS*, 480, 2963
- Oppenheimer, B. D., Crain, R. A., Schaye, J., et al. 2016, *MNRAS*, 460, 2157
- Papovich, C., Labbé, I., Quadri, R., et al. 2015, *ApJ*, 803, 26
- Peeples, M. S., Werk, J. K., Tumlinson, J., et al. 2014, *ApJ*, 786, 54
- Peng, C. Y., Ho, L. C., Impey, C. D., & Rix, H.-W. 2010, *AJ*, 139, 2097
- Phillips, A. C., Miller, J., Cowley, D., & Wallace, V. 2006, in *Proc. SPIE*, Vol. 6269, Society of Photo-Optical Instrumentation Engineers (SPIE) Conference Series, 62691O
- Pisano, D. J. 2014, *AJ*, 147, 48
- Planck Collaboration, Ade, P. A. R., Aghanim, N., et al. 2016, *A&A*, 594, A13
- Press, W. H., Teukolsky, S. A., Vetterling, W. T., & Flannery, B. P. 1992, *Numerical recipes in FORTRAN. The art of scientific computing*
- Rao, S. M., & Turnshek, D. A. 2000, *ApJS*, 130, 1
- Rubin, K. H. R., Prochaska, J. X., Koo, D. C., et al. 2014, *ApJ*, 794, 156
- Ruszkowski, M., Yang, H.-Y. K., & Zweibel, E. 2017, *ApJ*, 834, 208
- Salim, S., Rich, R. M., Charlot, S., et al. 2007, *ApJS*, 173, 267
- Sancisi, R., Fraternali, F., Oosterloo, T., & van der Hulst, T. 2008, *A&A Rv*, 15, 189
- Scannapieco, E., & Brüggén, M. 2015, *ApJ*, 805, 158
- Schawinski, K., Urry, C. M., Simmons, B. D., et al. 2014, *MNRAS*, 440, 889
- Schneider, E. E., & Robertson, B. E. 2017, *ApJ*, 834, 144
- Schneider, E. E., Robertson, B. E., & Thompson, T. A. 2018, *ApJ*, 862, 56
- Schroetter, I., Bouché, N., Wendt, M., et al. 2016, *ApJ*, 833, 39
- Shull, J. M. 2014, *ApJ*, 784, 142
- Sijacki, D., Vogelsberger, M., Kereš, D., Springel, V., & Hernquist, L. 2012, *MNRAS*, 424, 2999
- Sparre, M., Pfrommer, C., & Vogelsberger, M. 2019, *MNRAS*, 482, 5401
- Steidel, C. C., Kollmeier, J. A., Shapley, A. E., et al. 2002, *ApJ*, 570, 526
- Steidel, C. C., Shapley, A. E., Pettini, M., et al. 2004, *ApJ*, 604, 534
- Stern, J., Faucher-Giguère, C.-A., Hennawi, J. F., et al. 2018, *ApJ*, 865, 91
- Stewart, K. R., Brooks, A. M., Bullock, J. S., et al. 2013, *ApJ*, 769, 74
- Stewart, K. R., Kaufmann, T., Bullock, J. S., et al. 2011a, *ApJL*, 735, L1
- . 2011b, *ApJ*, 738, 39
- Strickland, D. K., Heckman, T. M., Weaver, K. A., & Dahlem, M. 2000, *arXiv, astro-ph*
- Su, K.-Y., Hopkins, P. F., Hayward, C. C., et al. 2018, *ArXiv e-prints*, arXiv:1809.09120
- Thompson, T. A., Quataert, E., Zhang, D., & Weinberg, D. H. 2016, *MNRAS*, 455, 1830
- Tumlinson, J., Thom, C., Werk, J. K., et al. 2011, *Science*, 334, 948
- van den Bergh, S. 1962, *AJ*, 67, 486
- Voit, G. M., Bryan, G. L., O’Shea, B. W., & Donahue, M. 2015, *ApJL*, 808, L30

- Voit, G. M., Meece, G., Li, Y., et al. 2017, *ApJ*, 845, 80
- Wang, B. 1995, *ApJ*, 444, 590
- Werk, J. K., Prochaska, J. X., Tumlinson, J., et al. 2014, *ApJ*, 792, 8
- Wizinowich, P., Le Mignant, D., Bouchez, A., et al. 2006, *PASP*, 118, 297
- Woolf, V. M., & West, A. A. 2012, *MNRAS*, 422, 1489
- Worthey, G., Dorman, B., & Jones, L. A. 1996, *AJ*, 112, 948
- Zabl, J., Bouché, N. F., Schroetter, I., et al. 2019, *MNRAS*, 485, 1961
- Zheng, Y., Putman, M. E., Peek, J. E. G., & Joungh, M. R. 2015, *ApJ*, 807, 103